Rapid formation of porphyry copper deposits evidenced by diffusion of oxygen and titanium in quartz

Federico Cernuschi[1]*, John H. Dilles[1], Stephanie B. Grocke[2], John W. Valley[3], Kouki Kitajima[3], and Frank J. Tepley III[1]

[1]*College of Earth, Ocean, and Atmospheric Sciences, Oregon State University, Corvallis, Oregon 97331-5506, USA*
[2]*Department of Mineral Sciences, National Museum of Natural History, Smithsonian Institution, Washington DC, 20560, USA*
[3]*Department of Geoscience, University of Wisconsin–Madison, Madison, Wisconsin 53706, USA*
*E-mail: fede@eclectic-rock.com

ABSTRACT

The lifespan of magmatic-hydrothermal activity that results in large and economically viable porphyry copper deposits remains poorly described. Here, we estimate the duration of the magmatic-hydrothermal fluid flow at 700 °C to <350 °C using diffusion profiles of Ti and $\delta^{18}O$ in quartz from Fe, Cu, and Mo sulfide-bearing hydrothermal veins and porphyry dikes at the Haquira East porphyry copper deposit, Peru. *In situ* measurements indicate all vein quartz is zoned in Ti (1–120 ppm), whereas high-temperature quartz has been re-equilibrated at 450 °C to $\delta^{18}O$ = 10.7‰. We use diffusion modeling to reproduce the observed Ti and $\delta^{18}O$ profiles, which provides lifespan estimates at Haquira of 75–170 k.y. for the period from initial magma and fluid injection at 700 °C to cooling below 350 °C. The bulk of the Cu-Mo-Au ore formed in ≤35 k.y., indicating that large-scale, economic porphyry copper deposits can form rapidly.

INTRODUCTION

Porphyry copper deposits are major Cu-Mo-Au producers, genetically related to shallowly emplaced arc-type granitoids (Data Repository[1]; Seedorff et al., 2005). Magmatic-hydrothermal fluids separate from magma and ascend by hydrofracturing the overlying wall-rock where they depressurize, cool from ~700 °C to <350 °C, and react with rock to form quartz veins and both vein-hosted and disseminated Fe, Cu, Mo, and Au-bearing sulfides. Significant Cu-ore resources require the emplacement and release of large volumes of fluid from a single magmatic intrusion (e.g., 4 Mt of Cu require >2 Gt of fluid; Data Repository). It remains unclear how rapidly this process occurs. U-Pb zircon ages of porphyry intrusions and Re-Os ages of hydrothermal molybdenite suggest fluid flow durations of ≤100 k.y. for the entire ore-formation process at Bingham (Utah, USA) and Bajo de la Alumbrera (Argentina; von Quadt et al., 2011), and for each of the several individual mineralizing fluid pulses at El Teniente (Chile; Spencer et al., 2015). Modeling of the widths and taper of alteration selvages yields shorter durations: ~100 yr for individual veins formed during sericitc alteration at Butte (Montana, USA; Geiger et al., 2002), and ~20 yr and ~900 yr for K-silicate alteration at Bajo de la Alumbrera and Butte, respectively (Cathles and Shannon, 2007). At Butte, diffusion modeling of Ti-in-quartz gradients in growth zones imaged by scanning electron microscope

cathodoluminescence (SEM-CL) suggest porphyry magma residence times of 1 k.y., and formation and cooling of various generations of hydrothermal vein quartz in 10 yr to 10 k.y. (Mercer et al., 2015).

We estimate the hydrothermal lifespan of the Haquira East porphyry Cu-Mo deposit (Peru) using SEM-CL images of quartz from porphyry dikes and veins, and *in situ* Ti and $\delta^{18}O$ compositions. Assuming Ti and $\delta^{18}O$ compositional gradients were initially abrupt step-like changes, we model the time to produce the gradients using experimental diffusivities, estimated temperatures, and cooling rates. The gradients of $\delta^{18}O$ in quartz analyzed by ion microprobe (SIMS) provide a novel approach to quantify time scales at low temperature (<400 °C) because oxygen isotope diffusivity is ~10,000 times faster than Ti diffusivity in quartz.

ORE GEOLOGY

Haquira East is a relatively deeply emplaced porphyry Cu-Mo-Au deposit (>8 km; see the Data Repository). It is hosted in a ca. 34 Ma subvertical granodiorite stock cut by a series of granodiorite porphyry dikes that are part of the Andahuaylas-Yauri batholith of southern Peru. Hydrothermal veins were emplaced in a regular sequence based on cross-cutting relationships (Fig. 1A; Cernuschi et al., 2013). We refer to various vein types using common conventions, as defined by Seedorff et al. (2005). Early aplite dikes are cut by sinuous and milky deep quartz veins (DQ) with traces of Cu-sulfides that are synchronous with porphyry dike emplacement. Younger EDM (early dark micaceous) alteration selvages contain biotite–muscovite–K-feldspar–bornite–chalcopyrite ± quartz. EDM selvages on fractures that rarely have quartz vein fill produce high-grade Cu ore, and are cut by banded molybdenite–quartz veins (BMQ) that introduce most of the Mo to the deposit. BMQ veins are cut by quartz veins that have a centerline infilled with bornite–chalcopyrite ± molybdenite and contribute Cu and Mo to ore (B veins). Quartz–muscovite–pyrite ± rare chalcopyrite veins with muscovite ± quartz ± pyrite alteration selvages cut all the earlier veins (D veins). Four Re/Os isotopic ages of molybdenite from BMQ veins average 33.75 ± 0.15 Ma, and one $^{40}Ar/^{39}Ar$ age of muscovite from a D vein yields 33.18 ± 0.21 Ma; these data provide a maximum lifespan of the Haquira hydrothermal system of ~600 k.y. (Cernuschi et al., 2013).

METHODS

Quartz in five polished sections was imaged using a FEI Quanta 600 field emission gun (FEG) scanning electron microcope (SEM) equipped with a Gatan MiniCL cathodoluminescence grayscale detector at Oregon State University (OSU, Corvalis, Oregon, USA; see the Data Repository for extended methods). The Ti content of quartz was measured using a CAMECA SX-100 electron microprobe (EMP; Table DR2 in the Data Repository) or by laser ablation–inductively coupled plasma–mass spectrometry (LA-ICP-MS; Table DR3) at OSU with detection limits of 13 and 0.2 ppm, respectively. CL grayscale images were processed with National Institutes of Health ImageJ software (https://imagej.nih.gov/ij/index.html) along line traverses, and calibrated using spot analyses of Ti. The $\delta^{18}O$ of quartz was analyzed *in situ* from 10-μm-diameter spots using a CAMECA IMS-1280 ion microprobe (SIMS) at the University of Wisconsin (Madison, Wisconsin, USA). Values are reported in per mil (‰) relative to Vienna Standard Mean Ocean Water (V-SMOW) with spot-to-spot precision of <0.3‰ (Tables DR4–DR9).

RESULTS

Five quartz samples (Table DR1; Figs. DR1 and DR2) selected based on vein cross-cutting relationships are representative of four progressively cooler thermal stages from early mineralizaton to post mineralization (Fig. 1A): a quartz phenocryst from a porphyry dike (Fig. 2); an EDM selvage re-opened by a B vein that is, in turn, cross-cut by late quartz in fractures (Fig. 3); a B vein rimmed by late quartz (Fig. 4); and two D veins (Fig. 5; Figs. DR3 and DR4).

The quartz phenocryst (Fig. 2) is CL-zoned, from core to rim, from light to dark gray (24–54 ppm Ti), and contains one internal band of bright CL and a second 10-μm-thick rim with ~75 ppm Ti. The bright CL of the phenocryst rim is similar to quartz in the adjacent aplitic porphyry groundmass (Fig. 1), and to hydrothermal quartz in DQ and BMQ veins.

The chalcopyrite-bornite–bearing EDM selvage envelopes a vein of mosaic-textured, uniformly gray-CL quartz with 24–47 ppm Ti that is crosscut by a B vein composed of strongly CL-banded quartz growth zones infilled by slightly later bornite-chalcopyrite (Fig. 3). B vein quartz is generally euhedral, with alternating gray-CL and bright-CL growth bands that range from 31 to 53 ppm Ti and from 69 to 84 ppm Ti, respectively. The $\delta^{18}O$ of quartz in gray-CL and bright-CL from all EDM and B vein bands is indistinguishable (mean of 10.67 ± 0.36‰; Fig. 3C).

Euhedral quartz from a different B vein sample (Fig. 4) also displays bright-CL (92–114 ppm Ti) and gray-CL (39–59 ppm Ti) growth bands with indistinguishable $\delta^{18}O$ compositions (mean of 10.40 ± 0.44‰; Fig. 4C). B vein quartz is fractured, partially dissolved, and then overgrown by rims and fracture-fillings of dark-CL quartz (<13 ppm Ti, below EMP detection limit; Fig. 4A). Dark-CL quartz has higher $\delta^{18}O$ compositions (mean of 12.49 ± 0.94‰; Fig. 4C) than B vein quartz.

A late D vein (Fig. 5) contains weakly growth-zoned, medium gray-CL quartz with 13–25 ppm Ti that is locally overgrown by dark-CL quartz with 1–6 ppm Ti (LA-ICP-MS). In D veins, the $\delta^{18}O$ of medium-gray CL quartz ranges from 9.7‰ to 12.6‰ (mean of 11.16 ± 1.45‰), and the dark-CL quartz ranges from 10.8‰ to 14.4‰ (mean of 12.57 ± 1.82‰). The medium gray-CL and dark-CL D vein quartz is similar in CL and isotopic composition to late quartz that fills fractures (Fig. 3B) and rims quartz in all early veins (DQ through B; Fig. 4B). Two spot analyses within fracture-filling quartz in an EDM vein yield $\delta^{18}O$ of 12.4‰ and 11.3‰ (Fig. 3C) and four additional spot analyses within a B vein range from 11.05‰ to 13.14‰ (Table DR4).

In summary, all quartz contain Ti diffusion profiles documented by variable CL intensity and correspondingly varied Ti contents of spot analyses. Early quartz in the EDM and B veins have relatively low and homogeneous $\delta^{18}O$ compositions of ~10.6‰. In contrast, the medium-gray and dark-CL quartz in the later D veins and fractures have relatively high $\delta^{18}O$ compositions of ~11.2 and 12.5, respectively.

DISCUSSION

Formation Temperature

Formation temperatures were estimated by the TitaniQ geothermometry of Huang and Audétat (2012). The observed bright-CL and high-Ti quartz is interpreted to result

from enhanced incorporation of Ti in crystal defects during non-equilibrium rapid quartz growth triggered by magmatic degassing during ascent. High growth rates of quartz yield spuriously high formation temperatures, by up to 100 °C (Huang and Audétat, 2012); therefore, we use the lowest Ti contents of quartz to estimate temperature.

Assuming crystallization in a magma chamber below the ore zone at ~300 MPa, the gray-CL outer part of the igneous quartz phenocryst (24–54 ppm Ti; Fig. 2) yields a TitaniQ temperature of 650–703 °C. Fluid inclusions in all veins are liquid + vapor, indicating trapping pressures >140 MPa at near-lithostatic conditions (see the Data Repository). Using 140 MPa pressure and the lowest Ti contents of quartz, EDM veins (27–49 ppm Ti) and B veins (18–59 ppm Ti) yield TitaniQ temperatures of 566–621 °C and 543–640 °C, respectively. D veins likely formed at near-hydrostatic pressure (~110 MPa), in which case medium-gray CL quartz (13–25 ppm Ti) and dark-CL quartz (1–6 ppm Ti) have TitaniQ temperatures of 494–546 °C and 343–441 °C, respectively. We consider all estimates maxima because of the Ti-in-quartz growth rate issue, and use conservatively low temperatures for isothermal diffusion models consistent with selvage mineral phase equilibria (i.e., 650 °C for magmatic quartz, 500 °C for EDM veins, 550 °C for B veins, and 450 to 350 °C for D veins; Seedorff et al., 2005; Table DR5).

Diffusion Models

We modeled isothermal diffusion in four quartz samples to calculate the lifespan of four thermal stages (650 °C, 550 °C, 450 °C and 350 °C) that represent the cooling of the magmatic-hydrothermal fluid from K-silicate to sericitic alteration (Fig. 1A). For each quartz type, we used the minimum estimated temperature to model the maximum time scale (Table DR5). The preferred models were selected using the best χ-squared goodness-of-fit statistic, which was also used to estimate the error for each model (see the Data Repository, Table DR6, Figs. DR5–DR7, DR10, and DR11). We used the equation from Crank (1975) for one-dimensional diffusion, and the spherical diffusion equation for closely spaced fractures in quartz (see the Data Repository). We also modeled the same diffusion profiles using the constraint of cooling from 700 to 325 °C (Watson and Cherniak, 2015, Table DR7).

Time Scales

Stage 1: Magmatic and Main Cu-Mo Stage

The Ti-in-quartz gradient between the quartz phenocryst core and its rim (Fig. 2A) is interpreted to have formed during rapid porphyry emplacement, and therefore represents the earliest and highest-temperature stage of the magmatic-hydrothermal system (Fig. 1A). Porphyry dikes were sequentially cut by aplites, and DQ and BMQ veins that all contain similar bright-CL quartz formed at a temperature of ~650 °C. The Cu-rich EDM selvages have ages intermediate between DQ and BMQ veins and formed at a lower temperature of ~500 °C, which suggest at least one cycle of cooling followed by heating (Fig. 1A). A diffusion model calculated at ~650 °C for Ti gradients at the core-rim boundary of a porphyry quartz phenocryst indicates a maximum time scale of 35 k.y (±15 k.y.) for the porphyry to BMQ stage; linear cooling from 700 to 600 °C yields 14.9 k.y. (Fig. 2A; Figs. DR6 and DR7).

Stage 2: Second Cu-Mo Stage

B veins with Cu-Mo sulfides contain bright-CL and gray-CL growth-banded quartz with resorption surfaces that attest of several temperature/pressure fluctuations (Figs. 3B and 4B). Using a mean temperature of 550 °C, diffusion models for three B vein Ti gradients provide a maximum time scale of ~50 k.y. (+50/−30 k.y.); linear cooling from 600 to 475 °C yields 25.4 to 40.9 k.y. (Fig. 1; Figs. DR6 and DR7).

Stage 3: 450 °C $\delta^{18}O$ *Homogenization of Early High-Temperature Quartz*

We assume that magma-derived hydrothermal fluids had relatively uniform $\delta^{18}O$, and produced all veins types (cf. Reed et al., 2013). We calculate a $\delta^{18}O$ composition of parent magmatic-hydrothermal water of 7.5–8.0‰ based on observed quartz compositions (Table DR6), application of quartz-water fractionation factors at hydrothermal conditions (Zhang et al., 1989), and our estimated vein formation temperatures (Table DR8). Our calculations suggest that the earlier medium gray-CL quartz ($\delta^{18}O$ of ~11.2‰) and later dark-CL quartz ($\delta^{18}O$ of ~12.5‰) from D veins are in equilibrium with magmatic water ($\delta^{18}O$ = 7.5‰; Taylor, 1968) at 450 and 380 °C, respectively. These temperatures are in good agreement with independent estimates derived from phase equilibria and the TitaniQ geothermometer. In contrast, the quartz in both EDM and B veins have identical mean $\delta^{18}O$ values (~10.6‰) that are in equilibrium with 7.5‰ water at ~475 °C, a slightly lower temperature compared to estimates from phase equilibria and TitaniQ geothermometry (500–550 °C). We interpret that oxygen within EDM and B vein quartz diffusively homogenized at ~450 °C with magmatic water that penetrated along fractures, that likely result from contraction upon cooling and are infilled locally by later medium gray-CL quartz (Fig. 3A; Figs. DR8 and DR9). Nonetheless, Ti contents of high-temperature EDM and B vein quartz attest to little reequilibration at <450 °C because of the low Ti diffusivity (Fig. 3). We modeled spherical three-dimensional (3-D) oxygen diffusion, along the 3-D network of fractures and dissolution bands that are commonly spaced every 40–120 μm (20–60 μm radius, respectively; Fig. DR9). Time scales were calculated for $\delta^{18}O$ profiles at 450 °C for diffusion between a 7.5‰ magmatic water and B vein quartz that was originally 9.6‰ (Fig. 6). Spherical diffusion models yield time scales of 1 and 10 k.y. (+10/−4 k.y.) to re-equilibrate across a distance of 20 and 60 μm, respectively. We consider the latter as the maximum duration of this stage (Fig. 1).

Stage 4: Late Quartz in D Veins and Fractures

The fractures through early quartz that remained opened were later filled during cooling by dark-CL quartz. One dark-CL D vein contains quartz with 1–6 ppm Ti formed at ~350 °C (Fig. 5), a temperature also assumed to characterize the dark-CL quartz in microfractures (Fig. 3). Modeling the $\delta^{18}O$ diffusion profile of a late 12.7‰ dark-CL rim on earlier 10.7‰ B vein quartz gives a maximum time of 75 k.y. (+25/−15 k.y.) at 350 °C and 69 k.y. for linear cooling from 375 to 325 °C (Figs. 1 and 4B).

CONCLUSIONS

The lifespan of the magmatic-hydrothermal system of deeply emplaced (>5 km depth) porphyry copper deposits can be relatively short. The isothermal diffusion modeling presented here uses conservatively low temperature estimates that provide a maximum magmatic-hydrothermal lifespan of 170 k.y. (+100/–64 k.y.) for cooling from 650 to 350 °C across four thermal stages (Fig. 1A). The corresponding linear cooling from 700 to 325 °C provides even shorter estimates of 75–153 k.y. (Fig. 1A). Significant ore resources can form even more rapidly. At Haquira East, the bulk of the 4.2 Mt of Cu, 37,000 t of Mo, and 28 t of Au contained in the ore were formed during stage 1 in ≤35 k.y. (Fig. 1A), implying that >2 Gt of fluid was released in this same period.

During the ore-forming processes of stages 1 and 2, magmatic-hydrothermal fluids ascended, heated the wall rock, and effectively produced an enhanced geothermal gradient and K-silicate to transitional alteration (Figs. 1B and 1C). Stage 1 includes the initial DQ veins and aplites at ~650 °C, later Cu-rich EDM veins at ~500 °C, and then a thermal reversal to form Mo-rich BMQ veins at ~650 °C. Additional Cu-Mo ore, hosted in B veins, was formed during stage 2 in ≤50 k.y. upon cooling to 550 °C.

The post-ore-formation cooling history is included in stages 3 and 4, reflecting the degradation of the geothermal gradient, as a response to crystallization of the deep magma chamber source of porphyry dikes and the decline of the magmatic-hydrothermal fluid flux. In stage 3, the $\delta^{18}O$ of preexisting quartz was partially homogenized in ≤10 k.y. at ~450 °C and in stage 4, sericitic alteration occurred at ~350 °C in a period of ≤75 k.y. The latter duration likely includes regional slow cooling attending the deep emplacement of Haquira. We expect significantly shorter time scales for shallowly emplaced porphyry deposits (<5 km depth) that cool faster.

ACKNOWLEDGMENTS

We thank First Quantum Minerals Ltd. (Vancouver, Canada) and the U.S. National Science Foundation (NSF; grants EAR-1355590, EAR–1658823, EAR-1524336 and EAR-1447730) for making this research possible. We are indebted to Brendan Murphy, Chris Clark, David Cooke, Celestine Mercer, Daniele Cherniak, and one anonymous reviewer for their insightful reviews.

REFERENCES CITED

Cathles, L.M., and Shannon, R., 2007, How potassium silicate alteration suggests the formation of porphyry ore deposits begins with the nearly explosive but barren expulsion of large volumes of magmatic water: Earth and Planetary Science Letters, v. 262, p. 92–108, https://doi.org/10.1016/j.epsl.2007.07.029.

Cernuschi, F., Dilles, J.H., and Creaser, R., 2013, Hydrothermal alteration, SWIR-mineral mapping, vein distribution and age of the Haquira-East Cu-Mo porphyry, *in* Jonsson, E., et al eds., Mineral Deposit Research for a High-Tech World, Proceedings of the 12th SGA (Society for Geology Applied to Mineral Deposits) Biennial Meeting, Uppsala, Sweden, v. 2, p. 782–785.

Crank, J., 1975, The Mathematics of Diffusion (2nd edition): Oxford, UK, Clarendon Press, 414 p.

Geiger, S., Haggerty, R., Dilles, J.H., Reed, M.H., and Matthäi, S.F., 2002, The evolution of the early hydrothermal alteration at Butte, Montana: New insights from reactive transport modeling: Geofluids, v. 2, p. 185–201, https://doi.org/10.1046/j.1468-8123.2002.00037.x.

Huang, R., and Audétat, A., 2012, The titanium-in-quartz (TitaniQ) thermobarometer: A critical examination and re-calibration: Geochimica et Cosmochimica Acta, v. 84, p. 75–89, https://doi.org/10.1016/j.gca.2012.01.009.

Mercer, C.N., Reed, M.H., and Mercer, C.M., 2015, Time scales of porphyry Cu deposit formation: Insights from titanium diffusion in quartz: Economic Geology and the Bulletin of the Society of Economic Geologists, v. 110, p. 587–602, https://doi.org/10.2113/econgeo.110.3.587.

Reed, M., Rusk, B., and Palandri, J., 2013, The Butte magmatic-hydrothermal system: One fluid yields all alteration and veins: Economic Geology and the Bulletin of the Society of Economic Geologists, v. 108, p. 1379–1396, https://doi.org/10.2113/econgeo.108.6.1379.

Seedorff, E., Dilles, J.H., Proffett, J.M., Jr., Einaudi, M.T., Zurcher, L., Stavast, W.J.A., Johnson, D.A., and Barton, M.D., 2005, Porphyry deposits: Characteristics and origin of hypogene features, *in* Hedenquist, J.W., et al., eds., Economic Geology 100th Anniversary Volume: Littleton, Colorado, Society of Economic Geologists, p. 251–298.

Spencer, E.T., Wilkinson, J.J., Creaser, R.A., and Seguel, J., 2015, The distribution and timing of molybdenite mineralization at the El Teniente Cu-Mo porphyry deposit, Chile: Economic Geology and the Bulletin of the Society of Economic Geologists, v. 110, p. 387–421, https://doi.org/10.2113/econgeo.110.2.387.

Taylor, H.P., Jr., 1968, The oxygen isotope geochemistry of igneous rocks: Contributions to Mineralogy and Petrology, v. 19, p. 1–71, https://doi.org/10.1007/BF00371729.

von Quadt, A., Erni, M., Martinek, K., Moll, M., Peytcheva, I., and Heinrich, C.A., 2011, Zircon crystallization and the lifetimes of ore-forming magmatic-hydrothermal systems: Geology, v. 39, p. 731–734, https://doi.org/10.1130/G31966.1.

Watson, E.B., and Cherniak, D.J., 2015, Quantitative cooling histories from stranded diffusion profiles: Contributions to Mineralogy and Petrology, v. 169, https://doi.org/10.1007/s00410-015-1153-4.

Zhang, L.G., Liu, J.X., Zhoum, H.B., and Chen, Z.S., 1989, Oxygen isotope fractionation in the quartz-water-salt system: Economic Geology and the Bulletin of the Society of Economic Geologists, v. 84, p. 1643–1650, https://doi.org/10.2113/gsecongeo.84.6.1643.

FIGURES

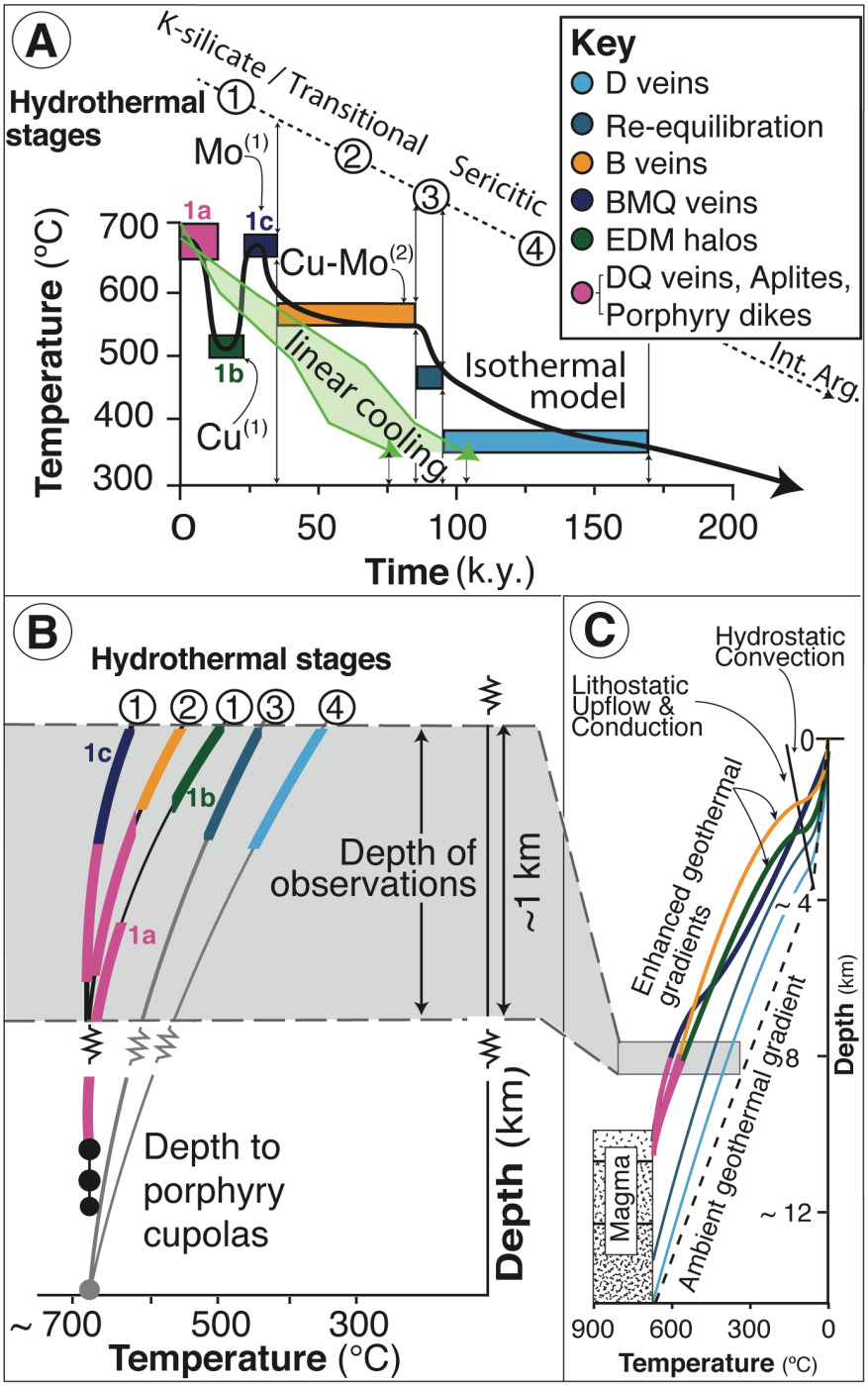

Figure 1. Summary of estimated time scales of the Haquira East porphyry Cu-Mo-Au deposit (Peru). A: Temperature and time evolution of the four hydrothermal stages and the formation of the Cu-Mo-ore. B,C: Schematic depth section illustrating the evolution of the geothermal gradient resulting from porphyry intrusions and fluid ascent. BMQ— banded molybdenite–quartz; EDM— early dark micaceous; DQ— deep quartz; Int.Arg.—Intermediate Argillic.

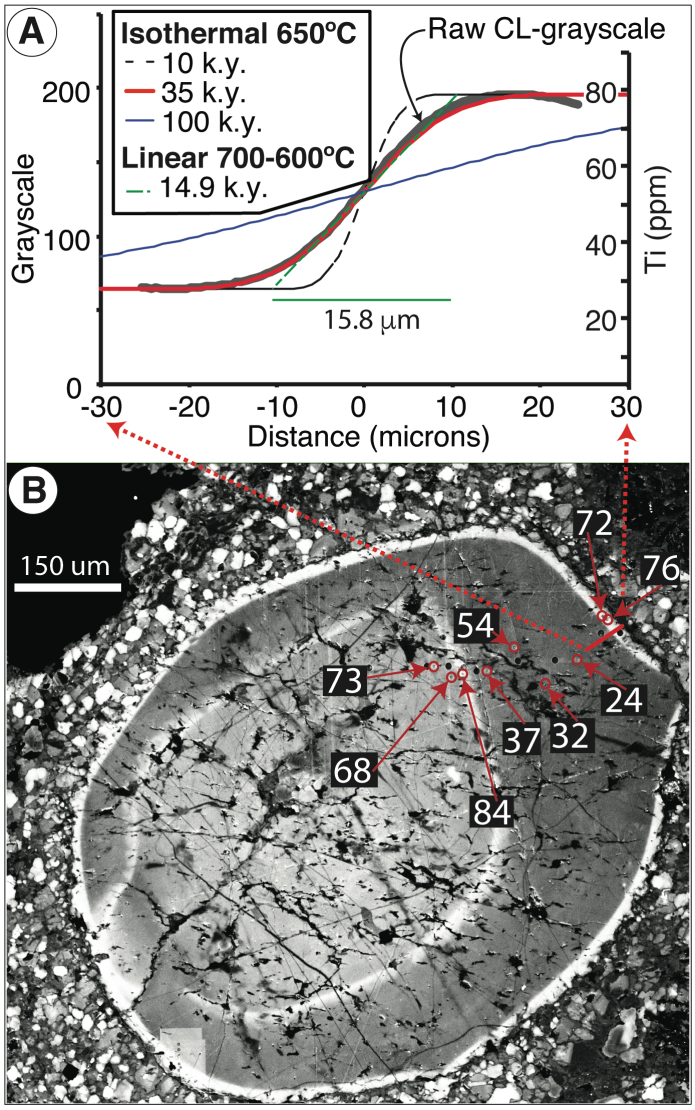

Figure 2. Scanning electron microscope cathodoluminescence (SEM-CL) image of a zoned quartz phenocryst in a porphyry dike composed of a light gray-CL inner core and a gray-CL outer core separated by a thin bright-CL band. A narrow bright-CL, high-Ti quartz band rims the gray-CL, lower-Ti outer core (B). A diffusion model calculated at ~650 °C for Ti gradients at the core-rim boundary indicates a maximum time scale of 35 k.y.

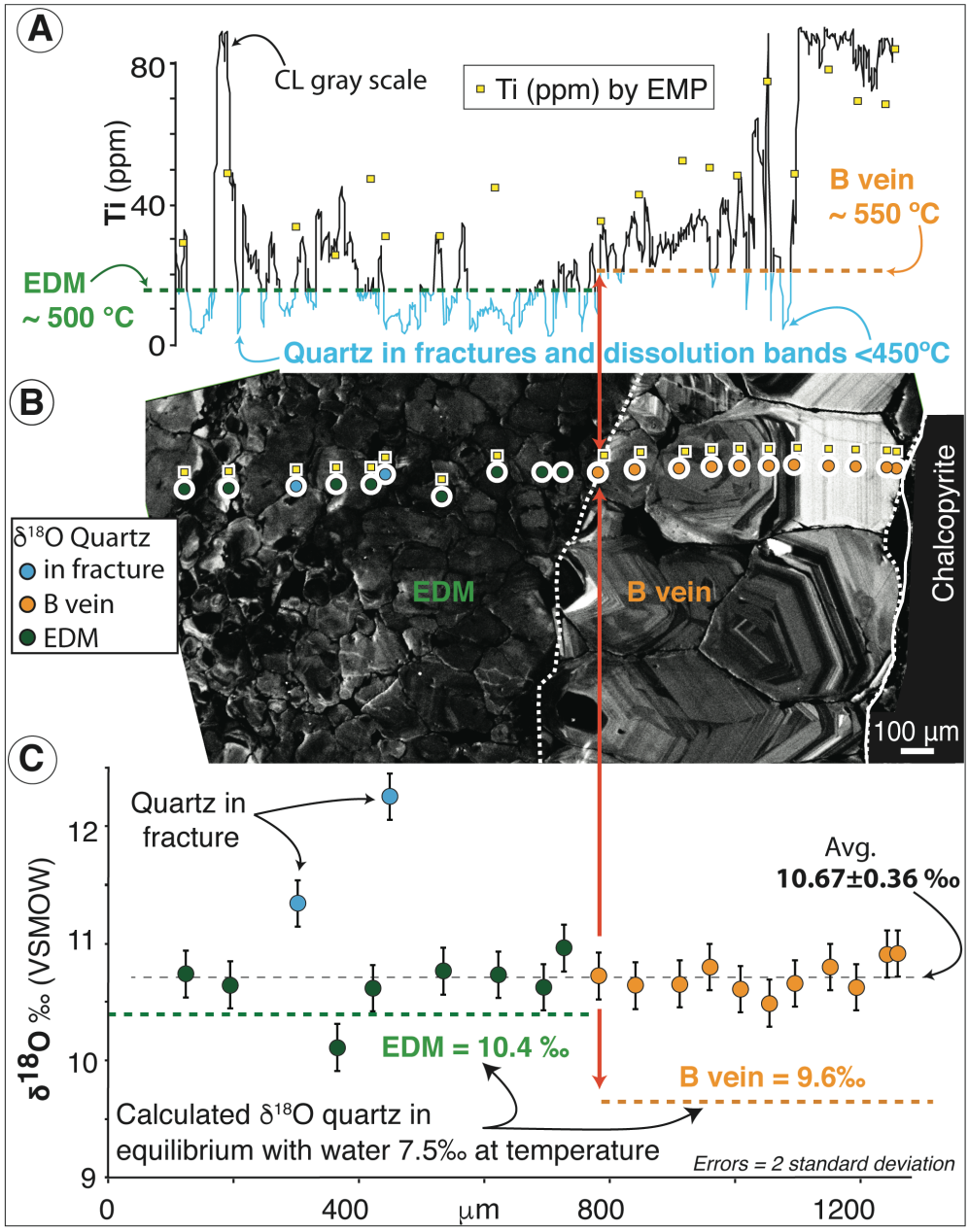

Figure 3. A: Ti-in-quartz data (electron microprobe, EMP) and cathodoluminescence (CL) grayscale profile along transect shown in B. TitaniQ temperature of EDM (early dark micaceous) and B vein quartz was calculated from the mean of the lowest Ti zones. B: SEM-CL of EDM gray-CL mosaic quartz re-opened and overgrown by gray- to bright-CL banded B vein euhedral quartz. C: Measured $\delta^{18}O$ ‰ (secondary ion mass spectrometry, SIMS) of quartz along the transect and calculated $\delta^{18}O$ ‰ based on the estimated temperature of precipitation (Table DR6 [see footnote 1]). VSMOW—Vienna Standard Mean Ocean Water.

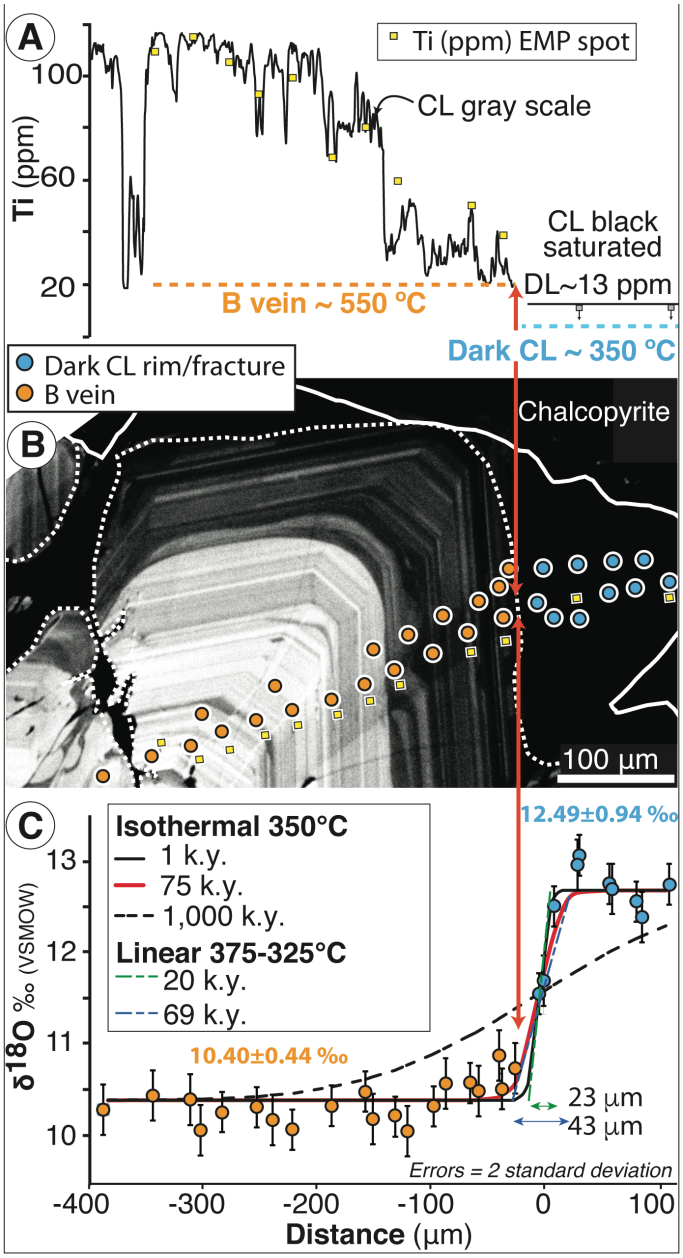

Figure 4. A: Ti-in-quartz data (electron microprobe, EMP) and cathodoluminescence (CL) grayscale profile along transect shown in B. Precipitation temperatures were calculated using the TitaniQ geothermometer of the lowest Ti zones. B: SEM-CL image of quartz illustrating inner, gray-CL zoned euhedral B vein quartz bands, two or more dissolution surfaces, and an overgrowth rim of later lower-temperature dark-CL quartz. C) $\delta^{18}O$ ‰ of quartz (secondary ion mass spectrometry, SIMS) along transect. B vein quartz varies from 10.1‰ to 10.7‰ whereas the dark-CL rim is ~12.7‰. The diffusion model for the observed $\delta^{18}O$ gradient between the B vein gray-CL quartz (10.1–10.7‰) and dark-CL rim (~12.7‰) suggests formation in ≤75 k.y. at ~350 °C. VSMOW—Vienna Standard Mean Ocean Water.

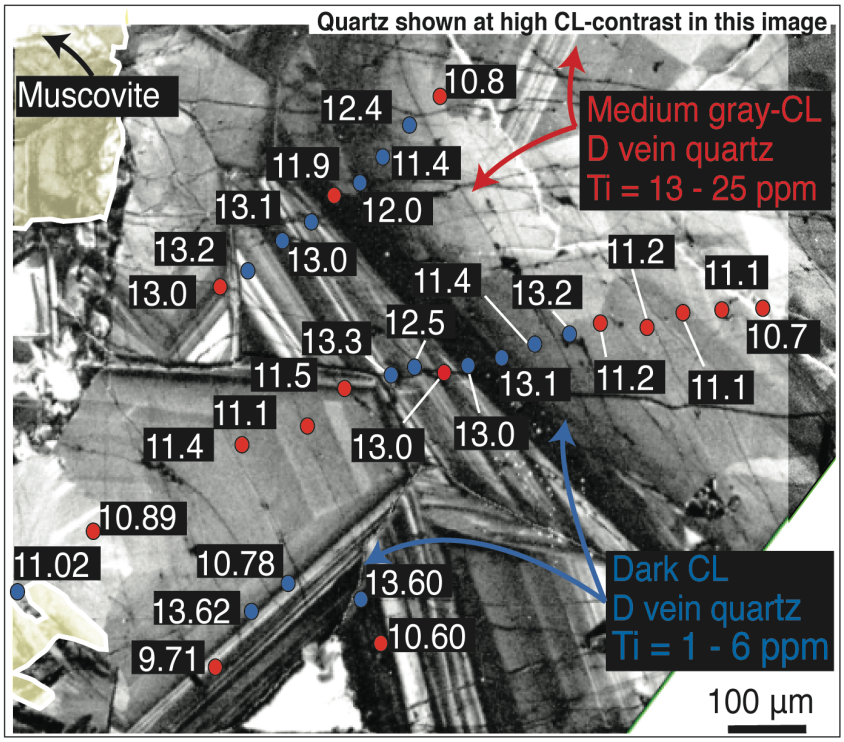

Figure 5. High-contrast scanning electron microscope cathodoluminescence (SEM-CL) image of quartz-muscovite-pyrite D vein. Quartz is euhedral and composed of bands of medium gray-CL (higher Ti, 10.8 < $\delta^{18}O$ < 13.6‰) and dark-CL (lower Ti, 9.7 < $\delta^{18}O$ <12.6‰).

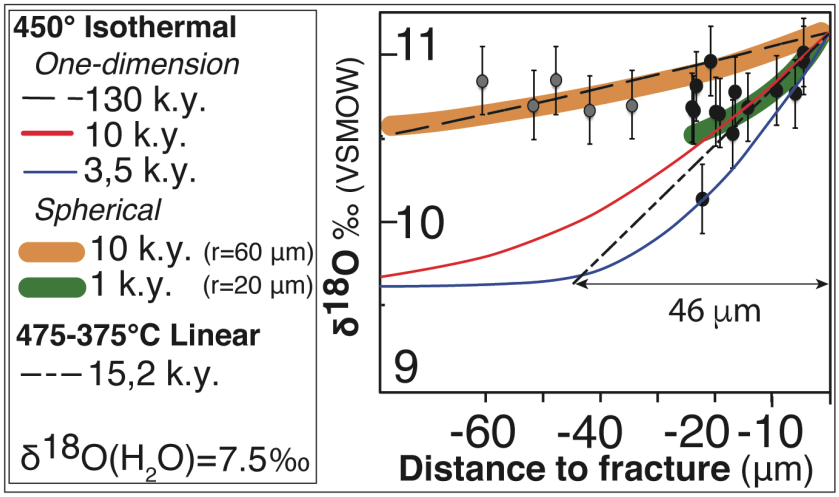

Figure 6. Quartz $\delta^{18}O$ ‰ (secondary ion mass spectrometry, SIMS) versus measured distance to fracture or dissolution band in a B vein (Fig. 2). Analyzed spots located at <20 µm and 30–60 µm from fracture/dissolution bands are black and gray, respectively. Spherical diffusion models yield 1 k.y. and 10 k.y. to re-homogenize quartz at <20 µm and <60 µm from fractures, respectively. VSMOW—Vienna Standard Mean Ocean Water, r — radius.

DATA REPOSITORY

Supplementary text, figures and tables to

"Rapid formation of porphyry copper deposits evidenced by diffusion of oxygen and titanium in quartz"

F. Cernuschi, J. H. Dilles, S. B. Grocke, J. W. Valley, K. Kitajima, and F. J. Tepley III

INDEX

Porphyry Cu±Mo±Au Deposits

Porphyry copper deposits include porphyry Cu±Mo±Au deposits in which copper is the chief economic metal. These deposits are large, ranging from <0.1 Mt (megatonnes) to >90 Mt contained copper, with ore grades ranging from <0.2 to >1.2 wt.% Cu with variable amounts of Mo and Au. The largest single deposit, albeit formed in multiple temporally spaced hydrothermal events introduced over several million years, is the El Teniente deposit, Chile (~96 Mt contained Cu), and perhaps the largest single hydrothermal event (<100,000 years; von Quadt *et al.,* 2011) is the Bingham, Utah, Cu-Au orebody (~28 Mt contained Cu). Porphyry copper deposits can be subdivided according to the tonnage of contained copper: <0.1 Mt Cu (small); 0.1 to 0.3162 Mt Cu (moderate); 0.3162 to 1.0 Mt Cu (large); 1.0 to 3.162 Mt Cu (very large); 3.162 to 10 Mt Cu (giant); 10 to 31.62 Mt Cu (supergiant); >31.62 Mt Cu (behemoths; Clark, 1993 and Cooke and Hollings, 2005).

In well-exposed porphyry deposits, a deep source intrusion, commonly estimated at >50 km^3 but as much as 500 km^3 (Ruby Star Granodiorite: Stavast *et al.,* 2008; El Abra Fiesta Granodiorite; Brimhall *et al.,* 2006; Dilles *et al.,* 2011) that is an equigranular granitoid is commonly exposed (see Burnham, 1979). These intrusions range from quartz diorite to granite to monzonite, and span the range from Na-rich to K-rich calc-alkaline to alkaline. Most intrusions are metaluminous, but some are weakly peraluminous or near the boundary of metaluminous to peralkaline (Seedorff *et al.,* 2005). The deep granitoid is the source of porphyry dikes of identical composition but with a porphyritic texture characterized by ~50 vol.% fine-grained groundmass that is commonly <0.1 mm in grain size, granitic in composition, and aplitic in texture. Such aplite represents a pressure-quench via water-vapor loss on ascent of magma at relatively low temperature (~700°C) (Burnham, 1979; Dilles, 1987). At Yerington and several porphyry deposits in the southwest of the USA, such porphyry dikes can be observed to grade downward into the deep granite, and moreover that younger dikes are more deeply sourced and cross-cut older dikes with slightly coarser groundmass (Dilles, 1987).

The formation of large and giant porphyry copper deposits requires the release of a large mass of magmatic-hydrothermal fluid from the source intrusion. This can be estimated by calculating the mass required to form the amount of quartz added in veins by hydrothermal fluids. To form the quartz veins observed in the Ann-Mason deposit in the Yerington district, 11 Mt of silica had to be transported by the hydrothermal fluid. This requires the release of 2.6 Gt of magmatic water from the Luhr Hill granite (Anne Schopa and John Dilles personal communication and Schopa *et al.,* 2017). According to Dilles (1987), the Luhr Hill granite volume can be estimated in 80 km^3 of magma or 200 Gt. The water content of the granite is ~ 4 wt. %, therefore, the granite hosted ~ 8 Gt of magmatic fluid. The amount of Cu lost from the 200 Gt Luhr Hill granite was estimated in 50 ppm, therefore, the 8 Gt of released fluid could have form up to 10 Mt of Cu. This estimate suggests that the released fluids from the granite may have formed the ~ 8 Mt PCD ore hosted in the district. In summary, at least 2Gt of fluid are required to form ~4Mt of Cu-ore.

As reviewed by Seedorff *et al.* (2005), porphyry deposits may form at a variety of depths in the upper crust ranging from as shallow as ~1 km for copper mineralization (*e.g.*, Batu Hijau, Yerington Mine) to ~10 km (*e.g.*, Butte, Montana; 6-8 km). Shallow deposits are characterized by "A" type granular quartz-sulfide veins, whereas deep deposits lack these veins but instead contain early dark micaceous (EDM) veins as at

Butte (Proffett, 2009). Shallower deposits likely form at slightly lower temperature and presumably may cool more quickly after fluid flow ceases. The range of observed hydrothermal temperatures in such deposits ranges from ~700°C at Butte (Brimhall, 1977; Field *et al.,* 2005; Rusk *et al.,* 2006; Mercer *et al.,* 2013) to about 300°C for late base metal veins associated with strong sericitic alteration (*e.g.* Rusk *et al.,* 2008; Landtwing *et al.,* 2005). Oxygen and hydrogen isotopic data suggest that all hydrothermal fluids that produce K-silicate and sericitic alteration are magmatic in origin at temperatures of 700 to 350°C (Harris and Golding, 2002; Zhang, 1995), consistent with thermal models of fluid flow (Weis *et al.,* 2012).

The Haquira East Porphyry Copper Deposit

The Haquira district contains two known porphyry copper centers. Haquira East is the focus of this study (-14.164877º, -72.345922º), and is the subject of the PhD thesis of Cernuschi (2015). Haquira East is a relatively large porphyry copper deposit with minor Mo and Au that contains measured, indicated, and inferred resources of 689 Mt ore containing 4.2 Mt Cu (~9 B lb), about 37,000 t Mo, and 28 t (0.9 M oz) Au (Antares, 2010). Haquira East is a relatively typical, but also a relatively deeply formed, porphyry copper deposit. A variety of evidence suggests Haquira formed at relatively great depth for a porphyry deposit. “A” type quartz veins are rare, and EDM veins are the largest contributors to Cu grades (Proffett, 2009; Cernuschi *et al.,* 2012). Late, low-temperature ~350 °C D pyrite-quartz veins with sericitic selvages and late <300 ºC pyrite veins with intermediate argillic alteration are rare (affecting <5% of the granodiorite porphyry stock). All observed fluid inclusions contain liquid and a moderate-sized vapor bubble, and were therefore trapped in quartz veins that formed at pressures greater than those that lead to fluid immiscibility (*i.e.* in the single-phase field); there are no observations of brine or vapor-rich inclusions indication fluid immiscibility. These inclusions were therefore trapped at >1.4 kb pressure. Fluid inclusion heating / freezing experiments provide homogenization temperatures and bulk salinities, which may be used together with appropriate P-T isochores, and comparison with Ti-in-quartz and phase petrology temperature estimates to estimate trapping pressures of between 1.6 kb and 3 kb at near-lithostatic pressures (Cernuschi, 2015). The fluid inclusion population more closely resembles the population at Butte, Montana where liquid plus vapor fluid inclusions dominate. However, at Butte fluid inclusions with trapped brines and vapors are rarely observed, and indicate that some fluid un-mixing occurred. Therefore, it is likely that Haquira East was emplaced at a greater depth than Butte where Rusk *et al.* (2008) estimated pressures of 2.0 to 2.5 kb for high temperature veins and a depth of emplacement of ~8 km.

Hydrostatic conditions must have prevailed at low temperatures below ca. 300-400°C in a zone that initially was above the Haquira East porphyry deposit but extended into the ore zones during formation of the late stage sericitic alteration and even later intermediate argillic alteration.

Moreover, geologic considerations also indicate great depth. Hornblende barometry of the nearby exposed and shallower Acojasa granodiorite pluton yields a pressure estimate of ~ 2 (±0.5) kb (Cernuschi, 2015, and references therein). The Acojasa and other associated intrusions are inferred to be concealed at depth below the meta-sedimentary succession that is preserved at Haquira East and are likely the source of the granodioritic stock, dikes and magmatic-hydrothermal fluids. One-kilometer deep drill-

holes did not reach the top of the inferred source intrusion below it. Therefore, the lithostatic pressure during the emplacement of Haquira East could have been > 2 kb. Furthermore, hornblende barometry of other intrusions in the Andahuyalas batholith at the Coroccohuayco Cu-skarn/porphyry deposit (Tintaya cluster) also yield high pressure, ranging from 1.4 to 2.4 Kbar (Chelle–Michou, 2013).

Nonetheless for purposes of this manuscript, we use conservative estimates of ~1.4 kb lithostatic pressure for high temperature hydrothermal conditions that transition to close to hydrostatic pressures at ~1.1 kb. Quartz phenocrysts (except the bright-CL rims) formed in an underlying magma chamber, so they likely formed at 2-3 kb pressure.

The Haquira East deposit is hosted in a granodiorite porphyry plug that intrudes a folded and ductile deformed quartzite sequence. Hydrothermal banded molybdenite-quartz (BMQ) veins cutting the quartzite are locally folded, and hydrothermal biotite in the porphyry plug is aligned into a foliation by deformation. This deformation does not affect the last porphyry dikes, which has an isotopic age that is indistinguishable from the earlier porphyries. Therefore, deformation was ongoing during porphyry emplacement, and suggests significant depth and >350°C for the rocks surrounding the deposit. As muscovite has a closure temperature to Ar diffusion of ~325-350°C (depending on grain size), the $^{40}Ar/^{39}Ar$ age of muscovite likely reflects slow cooling after the end of hydrothermal alteration. Hence, the hydrothermal lifespan is likely shorter than the 200,000 to 600,000 year interval defined by the Re-Os age of molybdenite and the $^{40}Ar/^{39}Ar$ age of muscovite. Average of 3 molybdenite ages is 33.75 ± 0.15 Ma and one $^{40}Ar/^{39}Ar$ age of muscovite yields 33.18 ± 0.21 Ma (Cernuschi *et al.,* 2013).

Extended Methods

Secondary Electron Microscope Cathodoluminescence (SEM-CL)

SEM-CL images of 30 and 200 μm thick polished sections were obtained at the Oregon State University Microscopy facility using a FEI Quanta 600FEG with a Gatan mini-CL detector with a wavelength range between 185 and 850 nm. Images were obtained while operating the instrument between 10 and 15 KeV, a spot size of 6 μm, scanning time between 50 and 200 μs and resolution of 1024x884 pixels. Thin sections were carbon coated or gold coated (< 100 nm thick) prior to the analyses. Gray scale profiles were obtained using NIH ImageJ software. For each profile the gray line shows the raw gray scale data and the black line represents a smoothed profile calculated by ImageJ. The smoothed profile is calculated by averaging contiguous pixel scale CL-intensity variations and is considered a better representation of the gray scale variations at the micron scale.

Electron Microprobe (EMP)

Titanium and aluminum in quartz on the thin section samples previously imaged by SEM-CL were obtained at Oregon State University using a CAMECA SX-100 Electron microprobe (EMP), by simultaneously collecting Ti x-rays on one LPET and two PET diffracting crystals, and collecting Al x-rays on one TAP and one LTAP diffracting crystals, a 15 keV accelerating voltage, a 200 nA beam current, a 1 um spot diameter and 600 second counting times on peak and 300 seconds on each background peak. Ti and Al detection limits of 13 ppm are calculated using three standard deviations of the counting rate for the background (3 sigma). With multiple diffraction crystals, this is the equivalent of 1800 seconds on peak and 900 seconds on each background peak for Ti, and 1200 seconds on peak and 600 seconds on each background peak for Al. We used rutile and as the primary standards for Ti and Al, and analyzed a Shandong quartz as a secondary standard (Shandong, Audétat *et al.,* 2014) routinely for Ti and Al concentrations between analyzes of unknown samples (Table A1). We obtained 58 ± 6 ppm Ti and 133 ± 7 ppm Al for 18 analyses of Shandong, which is comparable to the 57 ± 4 Ti ppm and 154 ± 15 ppm Al reported by Audetat *et al.* (2015).

Laser Ablation Inductively Coupled Plasma Mass Spectroscopy (LA-ICP-MS)

The LA-ICP-MS analyses at Oregon State University were obtained by using a Photon Machines Analyte G2 laser operating at 7 Hz with a 85 μm fixed spot and drilled to ~ 20 μm depth (Loewen and Kent, 2012; Dumitru et al., 2013). The total number of laser shot was 225 per analysis, with a pre-ablation shot count of 2. A He-Ar gas carried the ablated material to the plasma chamber and then into a Thermo XseriesII Quadrupole mass spectrometer, where the following elements were analyzed: ^{7}Li, ^{11}B, ^{23}Na, ^{27}Al, ^{28}Si, ^{31}P, ^{39}K, ^{47}Ti, ^{48}Ti, ^{49}Ti, ^{55}Mn, ^{56}Fe, ^{65}Cu, ^{72}Ge, ^{85}Rb, ^{88}Sr, ^{205}Tl, ^{208}Pb. Trace element concentrations were standardized to NIST-612 (Jochum *et al.,* 2011), and ^{28}Si in stoichiometry quartz as an internal standard, using an Excel application (LaserTram, Kent *et al.,* 2004). Spot analyses that included melt or fluid inclusions or accidental analyses of other minerals (i.e. sericite in D veins) were discarded by monitoring P, Al, Si, K, Sr, Rb. NIST-616 (Jochum *et al.,* 2011) was analyzed in between unknowns as a secondary standard. Based on the reproducibility, ^{49}Ti was preferred over ^{47}Ti and ^{48}Ti and yields a detection limit of 0.2 ppm Ti (3 sigma on background, Table 2).

Secondary Ion Mass Spectrometer (SIMS)

In situ SIMS $\delta^{18}O$ measurements were made on the CAMECA IMS 1280 ion microprobe at the University of Wisconsin-Madison WiscSIMS lab. Values standardized with bracketing analyses of UWQ-1 quartz standard (Valley and Kita, 2009) are reported in per mil (‰) relative to V-SMOW with spot-to-spot precision of <0.3‰ (see Supp. 4: Table DR4). Oxygen isotope measurements were collected along several traverses with a 1.7-1.9 nA Cs^+ primary beam. Analyses spots were ~10 μm diameter and 1 μm deep. Operating and analytical conditions are described in detail by Kita *et al.* (2009); Valley and Kita (2009); and Ferry *et al.* (2010). Secondary ^{16}O, $^{16}O^1H^-$ and $^{18}O^-$ ions were measured simultaneously using three Faraday cup detectors (C, FC2 and H1, respectively). $^{16}O^1H^-$ ions were measured for monitoring OH in quartz and contaminant such as mineral inclusions. The duration of the analyses was 3-4 minutes and the working standard was UWQ1 quartz (12.33‰ ± 0.3‰ (2 SD); ± 0.1‰ (2SE): Kelly et al. (2007), Ferry *et al.* (2014) appendix A). The working standard was measured 4-5 times before and after every 10 to 15 unknown analyses on every sample. The 2 standard deviation error for each bracketing set of the UWQ1 analyses was 0.27‰, and is considered the internal error. The raw $^{18}O/^{16}O$ ratios and $\delta^{18}O$ data were corrected to VSMOW using 83 measurements of UWQ1 during the run with a mean of 5.75‰, and errors of 2SD = 0.44‰, and 2SE = 0.05‰. These standard procedures are described by Ushikubo *et al.* (2012); Nakashima *et al.* (2013) and Tenner *et al.* (2013) and Ferry *et al.* (2014). (Table DR3).

TitaniQ geothermometry

Formation temperatures were estimated by TitaniQ geothermometry of Huang and Audétat (2012).

$$\log \text{Ti (ppm)} = -0.27943 \cdot 10^4 / T - 660.53 \cdot (P^{0.35} / T) + 5.6459$$

T is the temperature in Kelvin
P is the temperature in Kbar

Ti activity was estimated as 1 for the hydrothermal quartz based on the presence of rutile in quartz veins, and as 0.65 for magmatic quartz based on estimates for analogous arc rocks (Walker *et al.,* 2013).

Diffusion Calculations

Isothermal diffusion expression:

a. One dimensional

$$C = C_o \operatorname{erfc}\left(\frac{X}{2\sqrt{Dt}}\right)$$

C_o is the composition of mineral region A
C is the composition at distance X in mineral region B
D is the diffusion constant
t is time
erfc = 1-erf (error function)

See Crank (1975) and Valley (2001) for additional information

b. Spherical

$$\frac{C - C_1}{C_0 - C_1} = 1 + \frac{2a}{\Pi r} \sum_{n=1}^{\infty} \frac{(-1)^n}{n} \sin\frac{n\Pi r}{a} \exp(-Dn^2\Pi^2 t/a^2)$$

C_o is the composition at the surface of the sphere
C_1 is the initial composition of the sphere
C is the composition at distance a
r is the radius of the sphere
D is the diffusion constant
t is time

See Crank (1975) for additional information

Linear cooling

$$\log S_0 = 2.504 - \frac{1}{2}\log D_0 - \log T_i + \frac{1}{2}\log E_a + \frac{1}{2}\log T + \left(26.11\frac{E_a}{T_i}\right)$$

$\log S_0$ is log of the slope
S_0 is the slope dC/dx (m)
E_a is the activation energy
D_0 is the pre-exponent fator for diffusion
T_i is the initial temperature

See Watson and Cherniak (2015) for additional information

Diffusion Constants (Arrhenius equations):

Experimental wet diffusivities are available at temperatures that overlap only with the upper range of porphyry hydrothermal quartz precipitation: 648 - 1200 °C for Ti (Cherniak *et al.,* 2007) and 515 - 850 °C for oxygen under hydrothermal conditions (Dennis, 1984). The Arrhenius equation and experimentally determined activation energies for diffusion parallel to the c-axis of quartz were used to model diffusion perpendicular to growth zones of quartz, which are mainly on $\{\mathbf{10\bar{1}1}\}$ pyramidal faces.

a. Titanium (perpendicular to c-axis)

$D_{Ti} = 7 \times 10^{-8} \exp(-273 \pm 12 \text{kJ mol}^{-1}/RT)\text{m}^2\text{sec}^{-1}$ (Cherniak *et al.,* 2007)

Experimental temperature range: 700 to 1150°C

b. Oxygen (perpendicular to c-axis)

$D_{oxygen} = 2.09 \times 10^{-11} \exp(-138.54 \pm 19.1 \text{kJ mol}^{-1}/RT)\text{m}^2\text{sec}^{-1}$ (Dennis, 1984)

Experimental temperature range: 515 to 850°C

Chi-Square goodness-of-fit test

Chi-Square (χ^2) is a standard statistical test (Borradaile, 2003) that can be used to evaluate how well a model reflects the data. We used this test to evaluate how the measured Ti and/or O contents compare with those which would be expected under the fitted diffusion model. In this way, the Chi-Square test provides an objective tool to select the model that best fits the data, instead of selecting the preferred model by a traditional and more subjective visual fit of the model to the data. The preferred model was selected in order to minimize the Chi-Square using the formula:

$$X^2 = \sum \frac{(\text{observed} - \text{expected})^2}{\text{expected}}$$

Whereas a small Chi-Square statistical test value means that the observed data fits the expected data well, a large Chi-Square statistical test means that the observed data fits the expected data in a poor manner. The absolute number of the Chi-Square test statistic has no intrinsic meaning; therefore, the goodness of fitness cannot be compared between models on different samples.

The Chi-Square test was also used to evaluate the error of each diffusion model. Minimum and maximum timescales (also expressed as ± errors of the preferred timescale), were estimated using the range of "acceptable" good fitness. The "acceptable" good fitness range is the range of timescales with similar calculated sum of Chi-Square. Outside this range, the sum of Chi-Square increases rapidly. The acceptable range can be visualized as inflexion points in the curve that results from plotting the sum of Chi-Square versus estimated timescales.

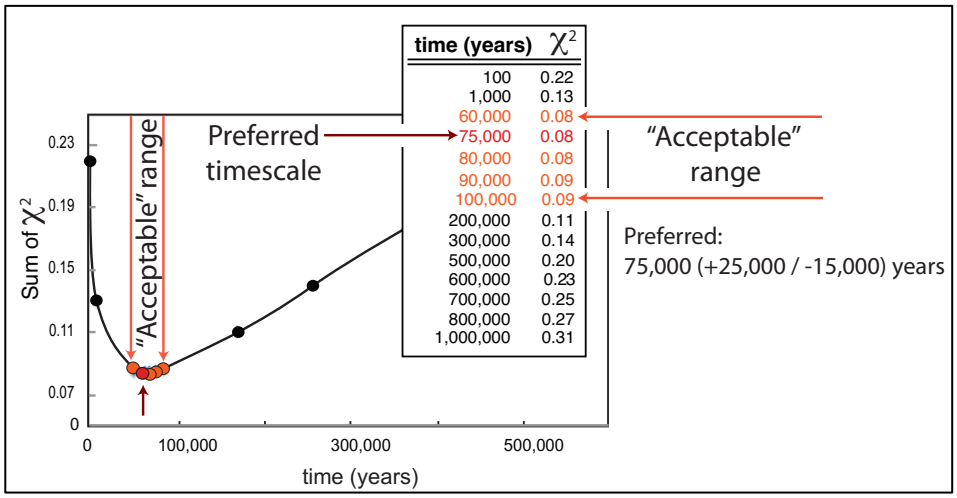

Figures

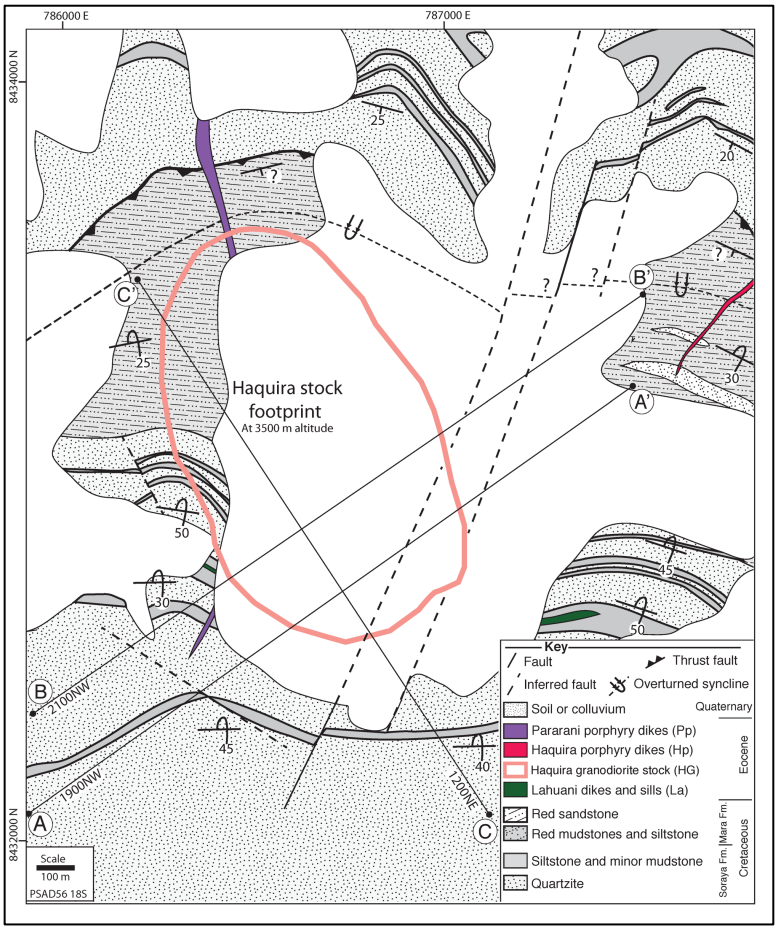

Figure DR1. Geologic map of Haquira East modified from Gans (2009) showing the location of cross-sections 1900NW, 2100NW and 1200NE (reproduced from Cernuschi, 2015). The footprint of the non-outcropping Haquira granodiorite stock is projected from a 3500 m altitude.

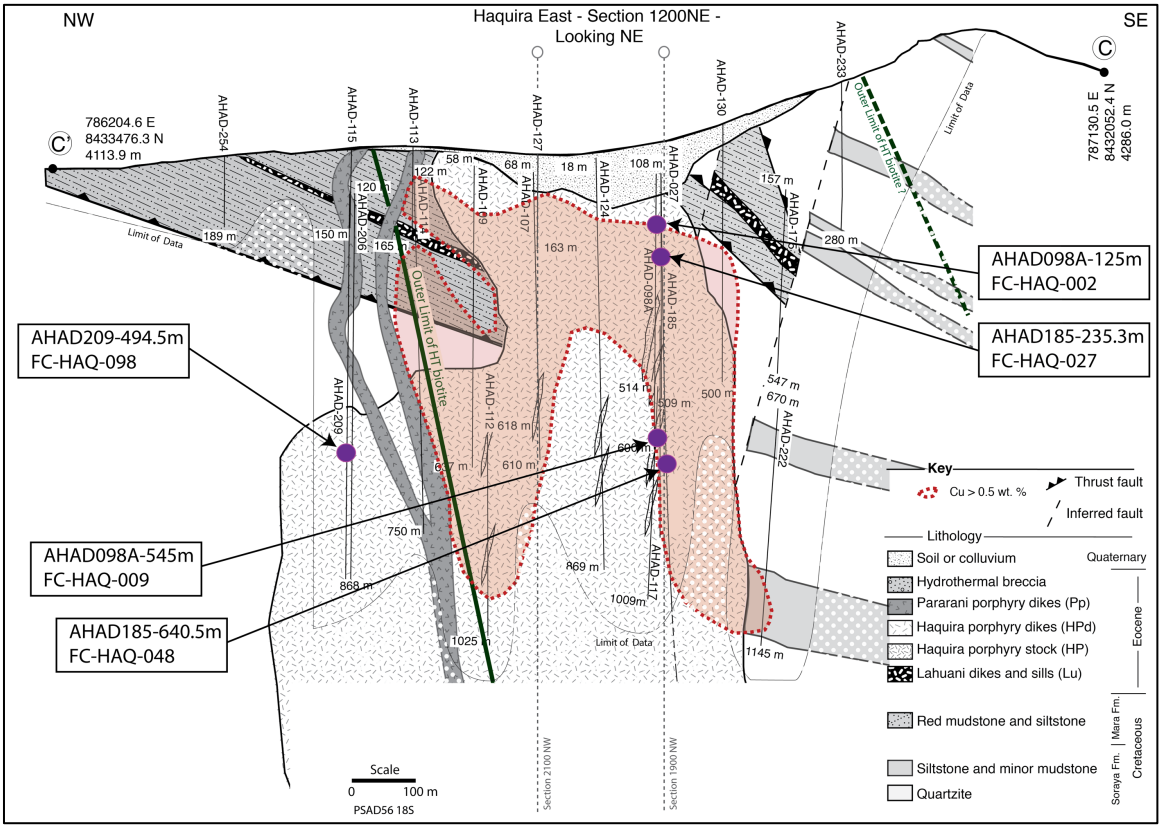
NW
Haquira East - Section 1200NE -
Looking NE
SE
C'
786204.6 E
8433476.3 N
4113.9 m
C
787130.5 E
8432052.4 N
4286.0 m
AHAD-254
AHAD-115
AHAD-113
AHAD-127
AHAD-130
AHAD-233
AHAD-206
AHAD-114
AHAD-109
AHAD-107
AHAD-124
AHAD-027
AHAD-177
AHAD-098A
AHAD-185
AHAD-209
AHAD-112
AHAD-222
AHAD-117
Limit of Data
Outer Limit of HT biotite
Outer Limit of HT biotite?
189 m
150 m
120 m
122 m
58 m
68 m
18 m
108 m
157 m
280 m
165 m
163 m
514 m
509 m
500 m
547 m
670 m
618 m
610 m
750 m
869 m
868 m
1009m
1025 m
1145 m
AHAD209-494.5m
FC-HAQ-098
AHAD098A-545m
FC-HAQ-009
AHAD185-640.5m
FC-HAQ-048
AHAD098A-125m
FC-HAQ-002
AHAD185-235.3m
FC-HAQ-027
Key
Cu > 0.5 wt. %
Thrust fault
Inferred fault
Lithology
Soil or colluvium
Hydrothermal breccia
Pararani porphyry dikes (Pp)
Haquira porphyry dikes (HPd)
Haquira porphyry stock (HP)
Lahuani dikes and sills (Lu)
Red mudstone and siltstone
Siltstone and minor mudstone
Quartzite
Quaternary
Eocene
Mara Fm.
Soraya Fm.
Cretaceous
Scale
0
100 m
PSAD56 18S
Section 2100 NW
Section 1900 NW

Figure DR2. Cross-section 1200NE (Cernuschi, 2015) showing location of analyzed samples in relation to the copper mineralization (>0.5 wt.% Cu) and K-silicate alteration illustrated by the extent of hydrothermal biotite after hornblende. The location of the cross-section is shown in Figure DR1.

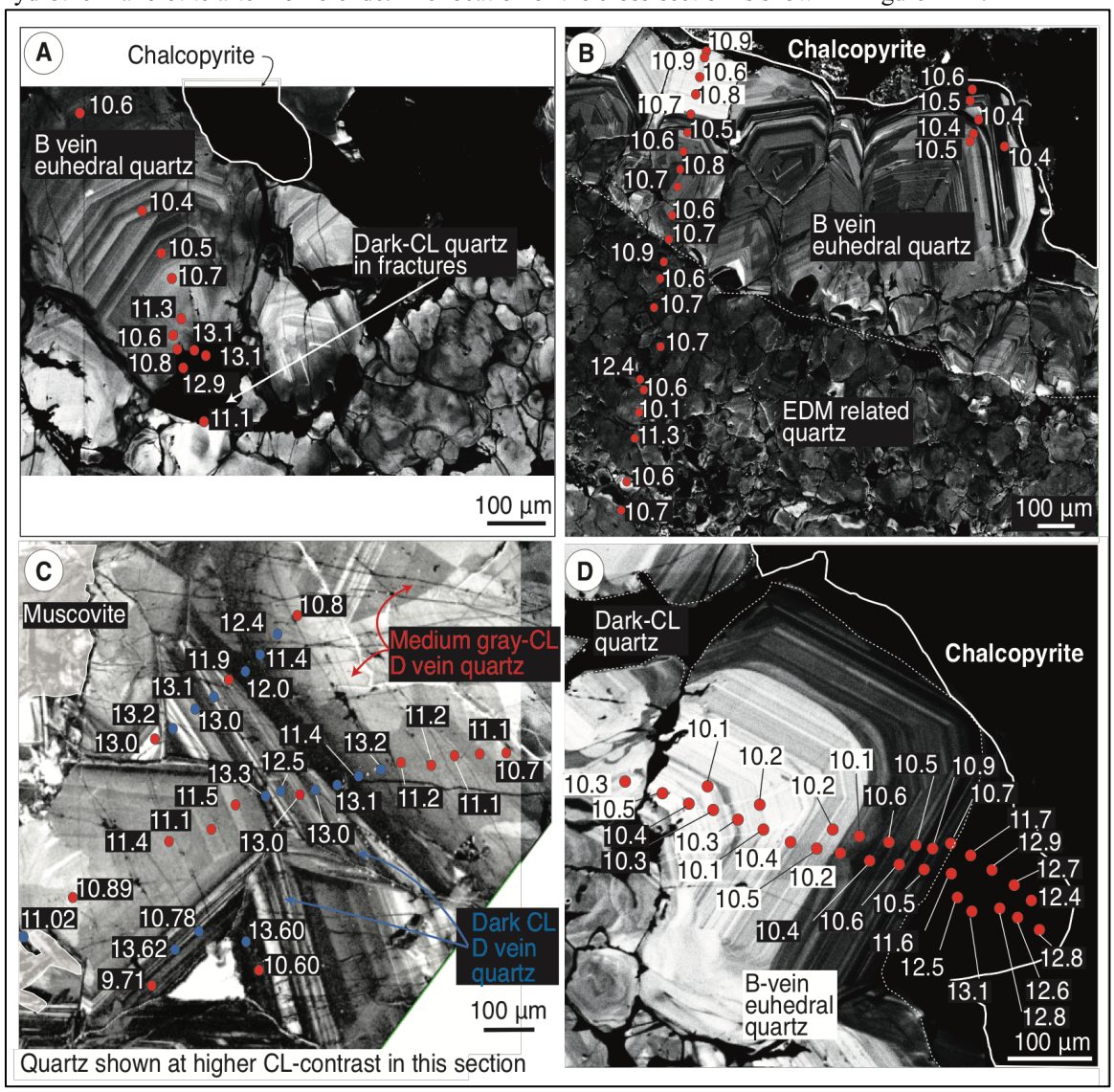

Figure DR3. $\delta^{18}O$ (‰) plotted on SEM-CL images of quartz from veins. A) B vein with chalcopyrite and late dark-CL quartz in fractures (FC-HAQ-048). B) Mosaic textured EDM related quartz overgrown by euhedral B vein quartz in contact with chalcopyrite (FC-HAQ-027). C) Euhedral quartz in D vein with

medium gray-CL quartz and dark-CL quartz growth zones in contact with muscovite and pyrite (FC-HAQ-009). D) Euhedral quartz in B vein rimmed by dark-CL quartz in contact with chalcopyrite (FC-HAQ-048).

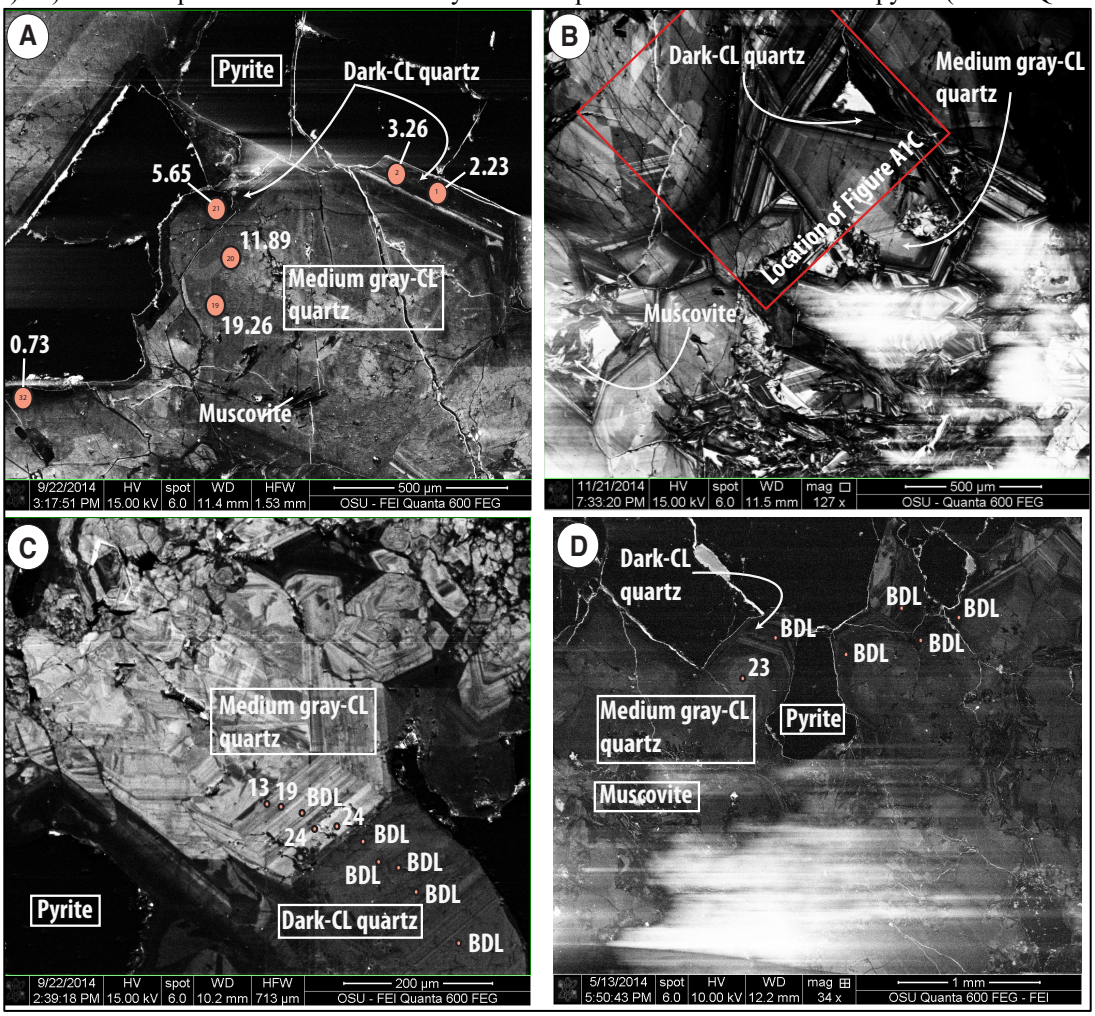

Figure DR4. Additional SEM-CL images of medium gray-CL and dark-CL quartz with muscovite and pyrite in D veins and spot location of Ti-in-Quartz data. A) FC-HAQ-098 with LA-ICP-MS spots in red showing Ti concentration. B) FC-HAQ-009, area shown in C is marked with a red square. C-D) EMP spots shown in red and indicating Ti concentration (BDL: below detection limit <13 ppm). C) FC-HAQ-098. D) FC-HAQ-009.

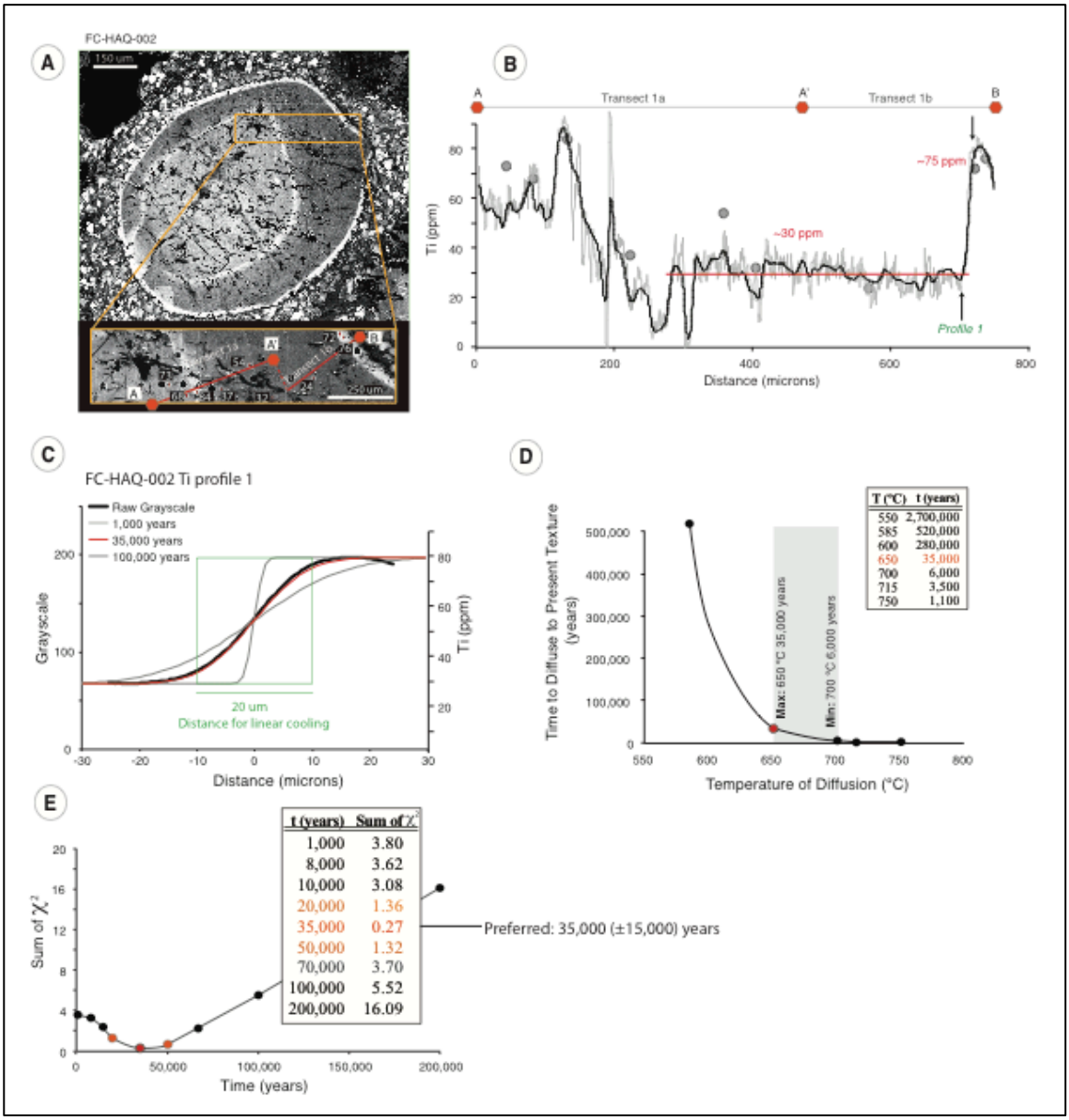

Figure DR5. A) Ti (ppm) in quartz spot analyses by EMP (Gray circles) and SEM-CL grayscale images for FC-HAQ-002. Insert shows the position of transects 1a and 1b. B) SEM-CL grayscale raw values (gray line) and smoothed grayscale (black lines) along transect 1a and 1b that are perpendicular to growth zones. Note the location of profile 1. C) Ti in quartz diffusion models for sample FC-HAQ-002 Profile 1. B) Modeled diffusion timescales versus temperature of diffusion used in the model at a fixed Sum of χ^2. The grey box shows the range of calculated diffusion timescales. The maximum timescale is the preferred. C) Sum of χ^2 versus time. The red circles show the preferred timescale based on the best fit of the model to the data as represented by the Sum of χ^2. The orange circles show the range of timescales that produce a reasonable fit of the model to the data as represented by a Sum of χ^2 smaller than 1.4.

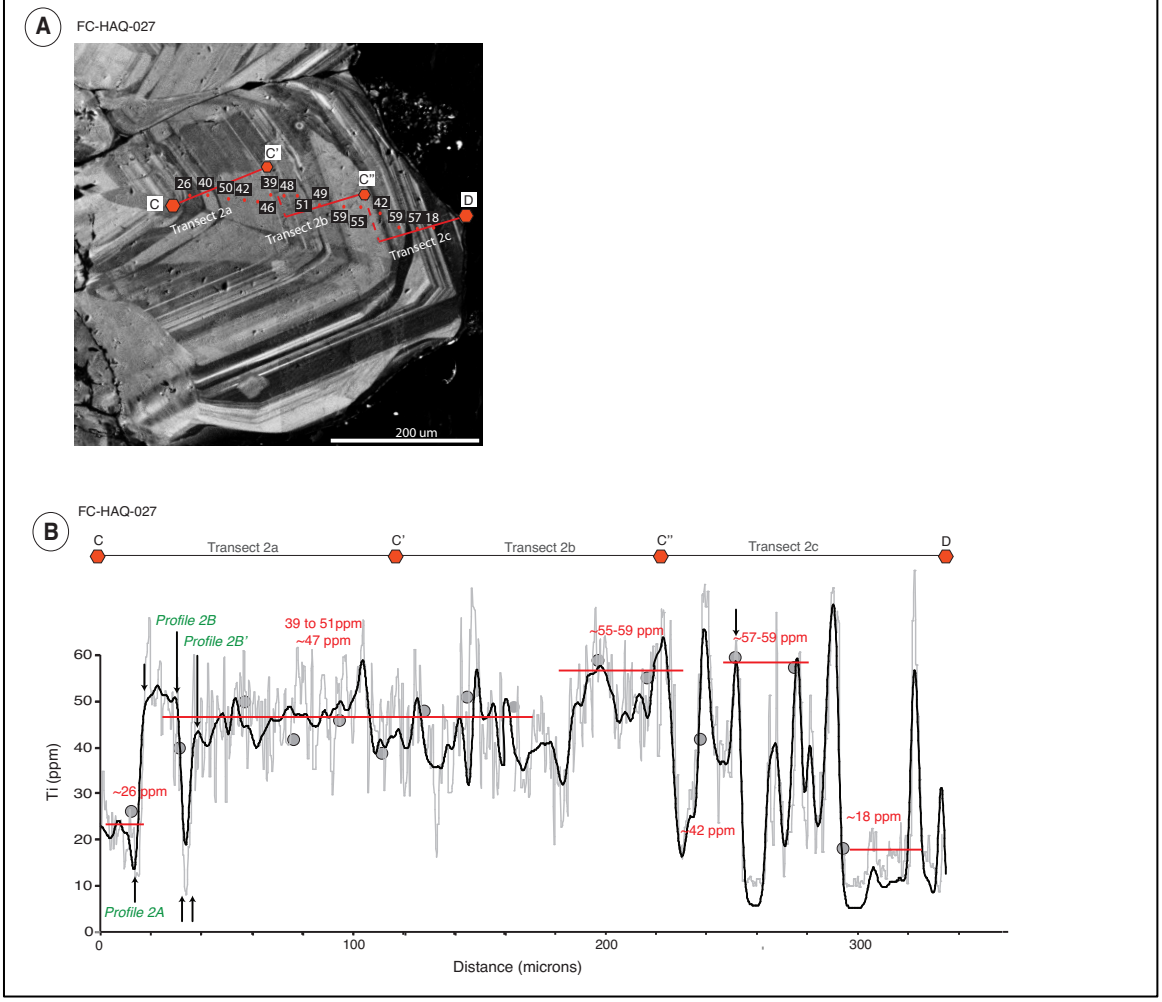
A
FC-HAQ-027
C
C'
C''
D
26 40 50 42
39 48
46
49
51
42
59 55
59 57 18
Transect 2a
Transect 2b
Transect 2c
200 um
B
FC-HAQ-027
C
Transect 2a
C'
Transect 2b
C''
Transect 2c
D
Profile 2B
Profile 2B'
39 to 51ppm
~47 ppm
~55-59 ppm
~57-59 ppm
~26 ppm
~42 ppm
~18 ppm
Profile 2A
Ti (ppm)
0
10
20
30
40
50
60
0
100
200
300
Distance (microns)

Figure DR6. A) Ti (ppm) in quartz spot analyses by EMP (Gray circles) and SEM-CL grayscale images for FC-HAQ-027. B) SEM-CL grayscale raw values (gray line) and smoothed grayscale (black lines) Note position of profiles 2A, 2B and 2B' (green-labels).

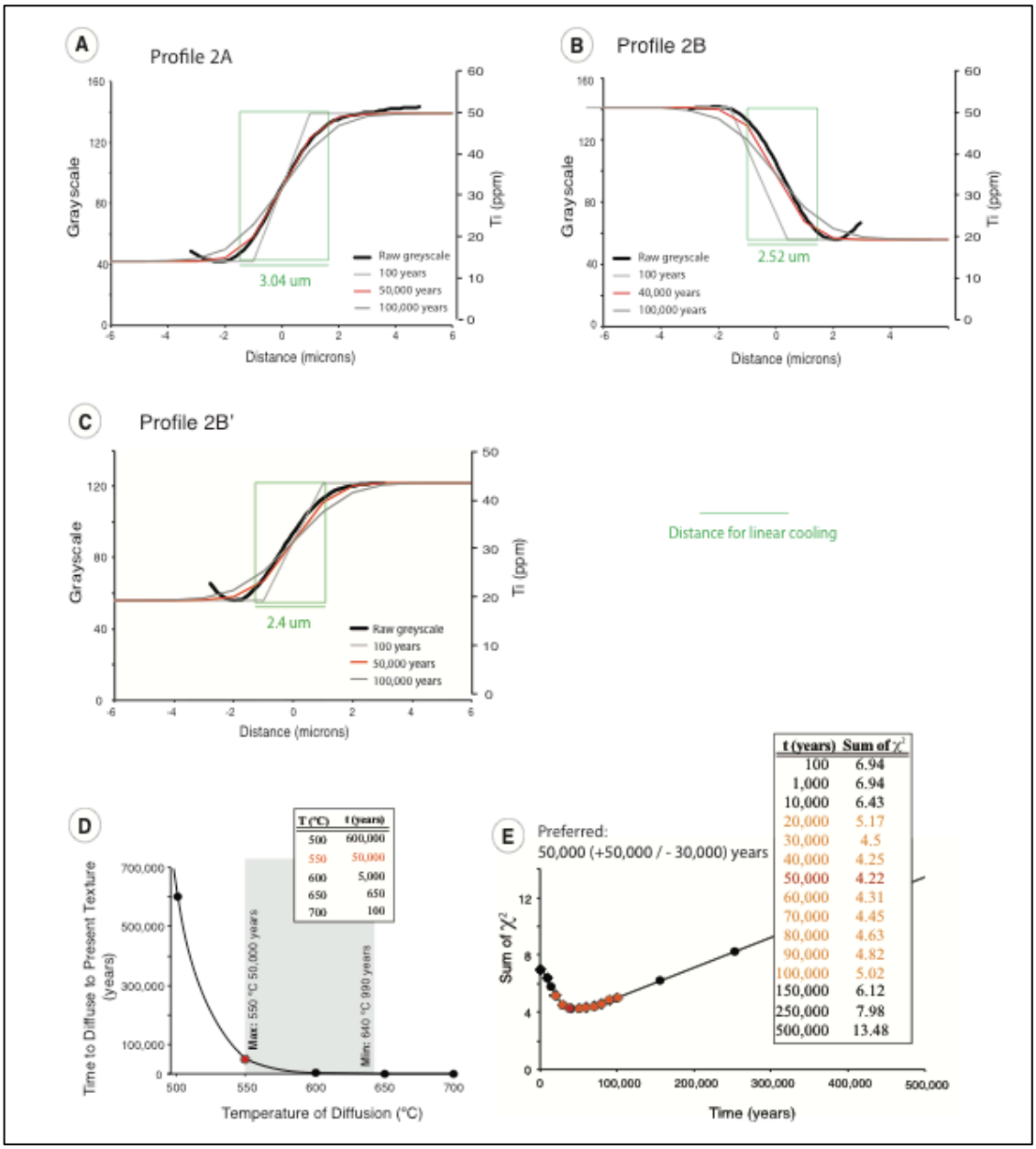

T (°C)	t (years)
500	600,000
550	50,000
600	5,000
650	650
700	100

t (years)	Sum of χ^2
100	6.94
1,000	6.94
10,000	6.43
20,000	5.17
30,000	4.5
40,000	4.25
50,000	4.22
60,000	4.31
70,000	4.45
80,000	4.63
90,000	4.82
100,000	5.02
150,000	6.12
250,000	7.98
500,000	13.48

Figure DR7. Ti in quartz diffusion models for sample FC-HAQ-027 (Figure DR6): A) Profile 2A, B) Profile 2B, and C) Profile 2B´. D) Modeled diffusion timescales versus temperature of diffusion used in the model at a fixed Sum of χ^2 for model of transect 2B'. The grey box shows the range of calculated diffusion timescales. The maximum timescale is the preferred. E) Sum of χ^2 versus time, for model of transect 2B'. The red circles show the preferred timescale based on the best fit of the model to the data as represented by the Sum of χ^2. The orange circles show the range of timescales that produce a reasonable fit of the model to the data as represented by a Sum of χ^2 smaller than 5.2.

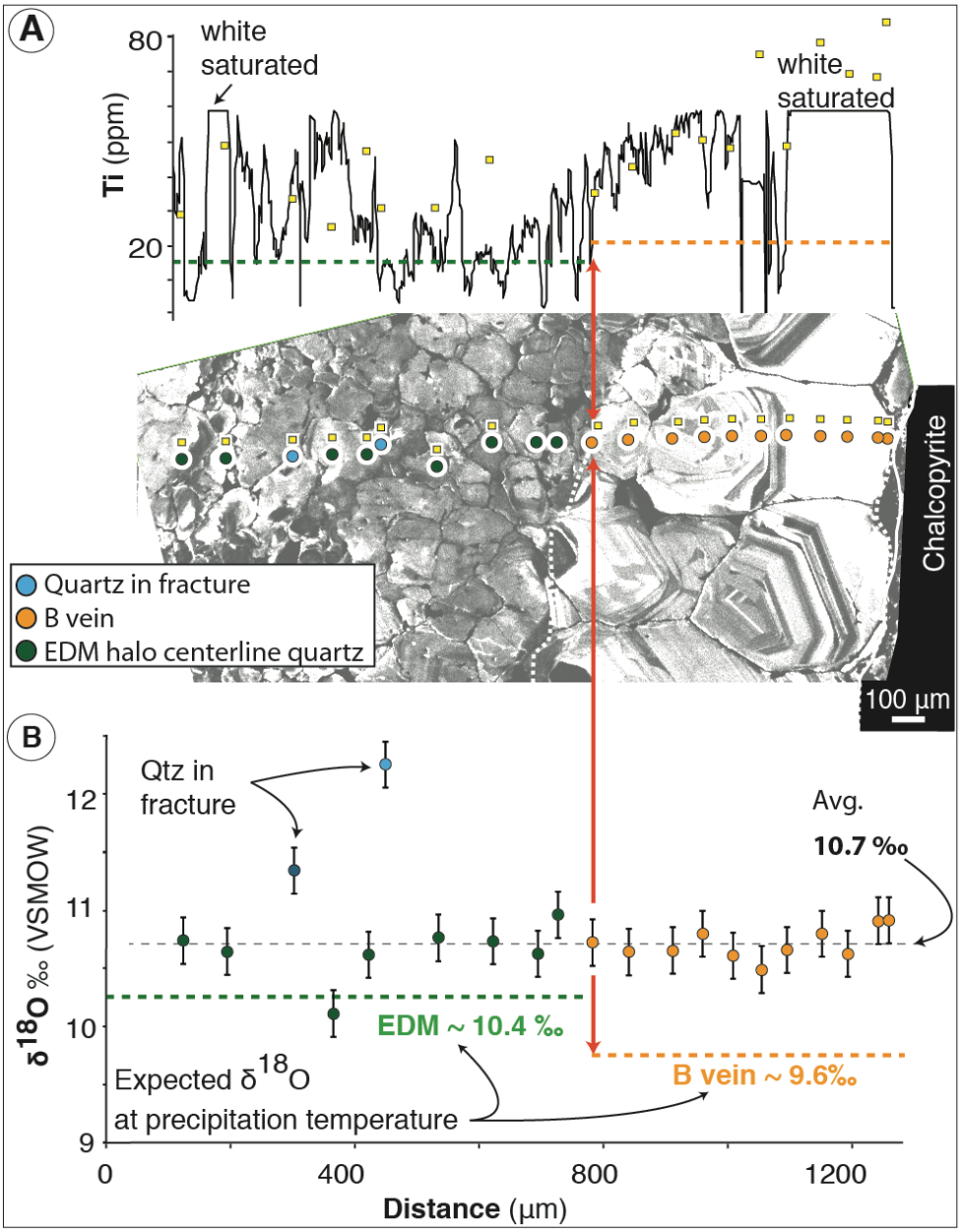

Figure DR8. Figure 3 in main text reproduced with SEM-CL image at higher contrast to highlight the fractures filled with late dark-CL quartz.

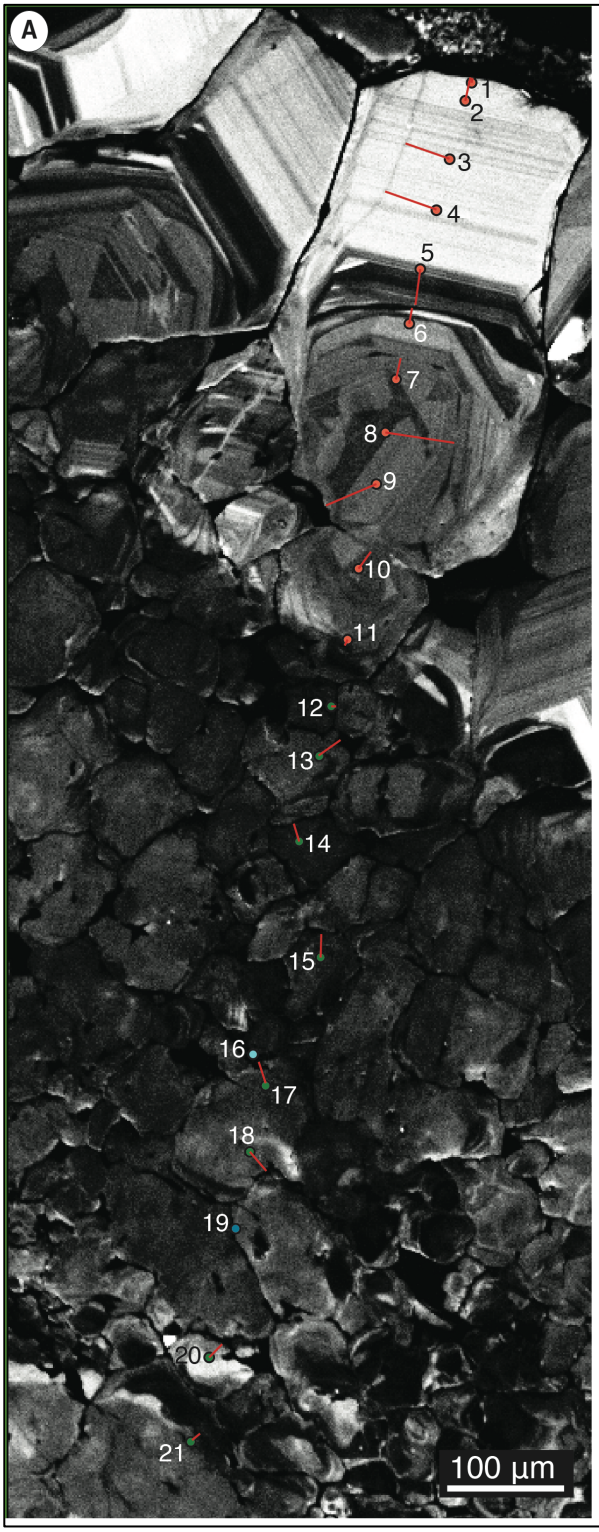

B

Spot #	$\delta^{18}O$ ‰ VSMOW	2SD	Distance (µm)
1	10.9	0.2	4
2	10.9	0.2	19
3	10.6	0.2	39
4	10.8	0.2	44
5	10.7	0.2	32
6	10.5	0.2	16
7	10.6	0.2	18
8	10.8	0.2	56
9	10.7	0.2	48
10	10.6	0.2	22
11	10.7	0.2	5
12	11.0	0.2	4
13	10.6	0.2	22
14	10.7	0.2	15
15	10.8	0.2	21
16	12.4	0.2	Fracture
17	10.6	0.2	18
18	10.1	0.2	20
19	11.3	0.2	Fracture
20	10.6	0.2	13
21	10.7	0.2	8

Figure DR9. Sample FC-HAQ-027. Distance from center of SIMS pits (see Figure DR8) to the closest fracture or dissolution band. Distance measured perpendicular from the fracture. A) SIMS pits on SEM-CL image. Pits color coded by quartz type (green = EDM, orange = B vein, light blue = late quartz in fractures (dark gray-CL and dark-CL). B) Summary table with distance to fracture or dissolution band.

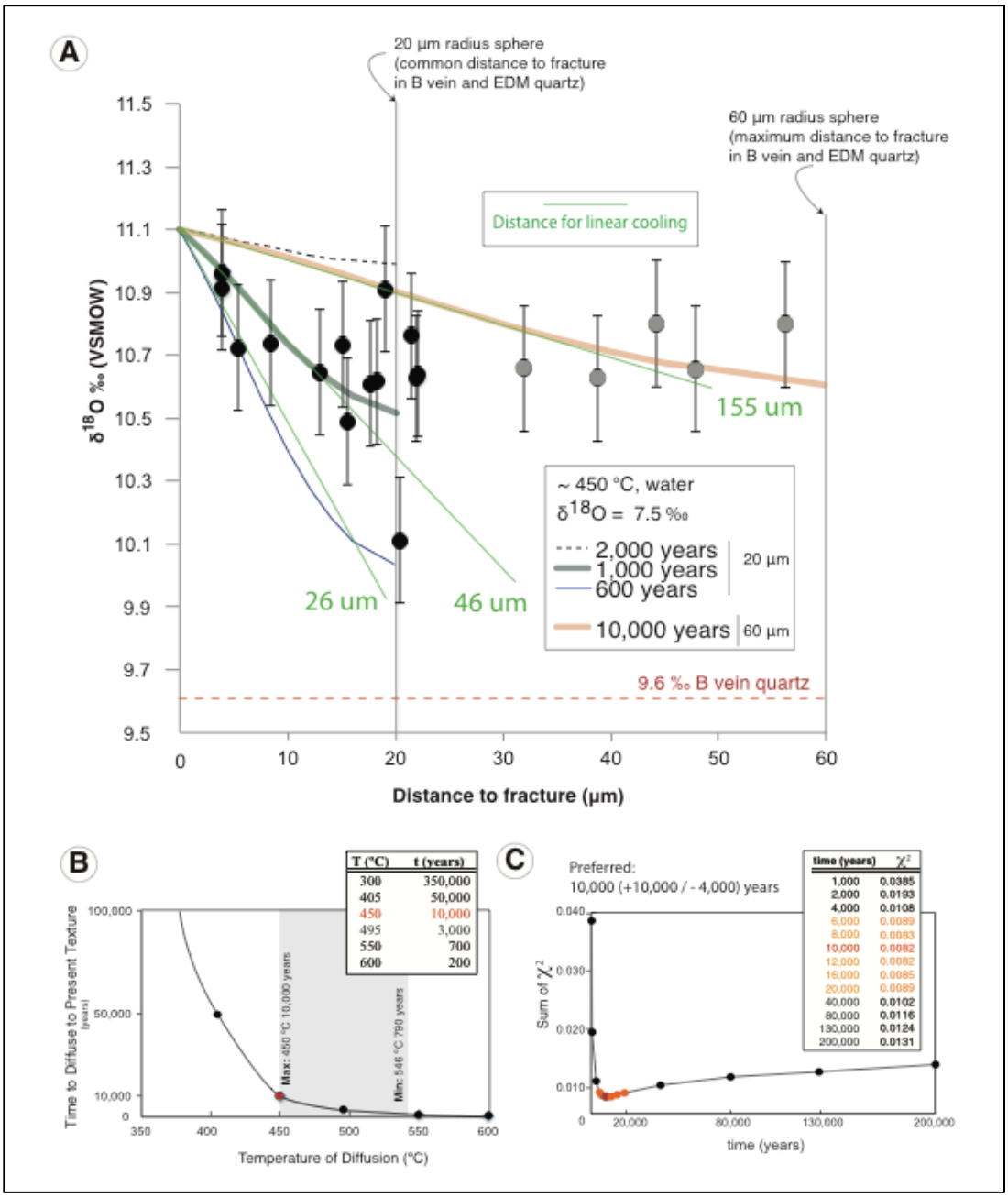

Figure DR10. A) Spherical diffusion models for partial re-equilibration of B vein and EDM quartz at 450 ºC (sample FC-HAQ-027, Figure DR8). Most of the measured distances from a SIMS-spot to the closest fractures or dissolution band are <20 µm (black dots). Partial re-equilibration can be achieved in ~1,000 years if fluid migrated through fractures spaced every 20 µm (green line). Some SIMS-spots are further away from fractures or dissolution bands. For these spots, the distances range from 20 µm to 60 µm (gray dots). These distances may be overestimates, if we assume that closely spaced fractures are present in other directions than in the observed surface. A partial re-equilibration of the quartz to the maximum measured distance to fracture (~60 µm) requires ~10,000 years (orange line). B) Modeled diffusion timescales versus temperature of diffusion used in the model at a fixed Sum of χ^2 the 10,000 year model. The grey box shows the range of calculated diffusion timescales. The maximum timescale is the preferred. C) Sum of χ^2 versus time. The red circles show the preferred timescale based on the best fit of the model to

the data as represented by the Sum of χ^2. The orange circles show the range of timescales that produce a reasonable fit of the model to the data as represented by a Sum of χ^2 smaller than 0.0090.

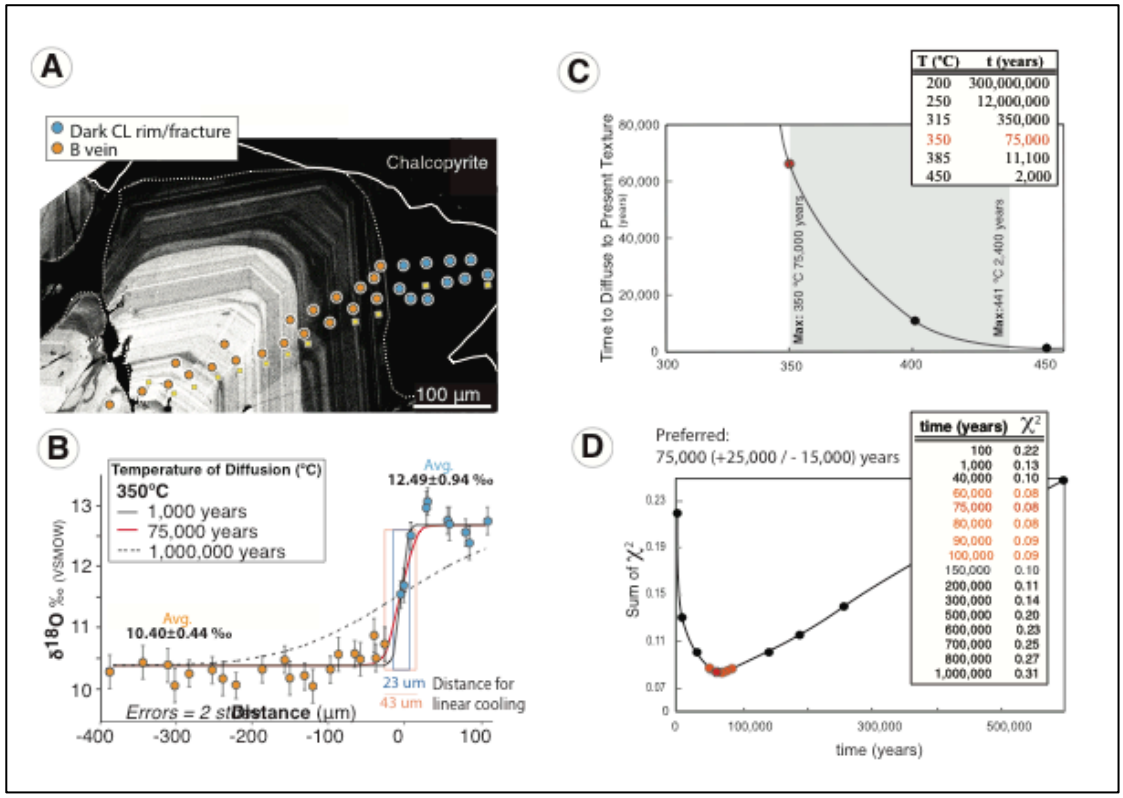

Figure DR11. A, B) Diffusion model shown in Figure 4 in the manuscript with distances used for linear cooling modelling. C) Modeled diffusion timescales versus temperature of diffusion used in the model at a fixed Sum of χ^2. The grey box shows the range of calculated diffusion timescales. The maximum timescale is the preferred. D) Sum of χ^2versus time. The red circles show the preferred timescale based on the best fit of the model to the data as represented by the Sum of χ^2. The orange circles show the range of timescales that produce a reasonable fit of the model to the data as represented by a Sum of χ^2 smaller than 0.09.

Tables

Table DR1. SAMPLE LOCATION

Sample	Drillhole	Depth (m)	Latitude	Longitude	Figure	Description
FC-HAQ-002	AHAD-098A	125.8	-14.16567	-72.34654	2	Quartz phenocryst
FC-HAQ-009	AHAD-098A	545			5	D vein
FC-HAQ-027	AHAD-185	235.3	-14.16678	-72.34653	3	EDM selvage with B vein and late quartz fractures
FC-HAQ-048	AHAD-185	640.5			4	B vein with late quartz rim
FC-HAQ-098	AHAD-209	494.5	-14.16678	-72.34653	DR4	D vein